Channel Morphological Activation of Large Braided Rivers in Response to Climate-driven Water and Sediment Flux Change in the Qinghai-Tibet Plateau

Yucong He[1], Zhiwei Li[2], and Yinjun Zhou[3]

[1] State Key Laboratory of Water Resources Engineering and Management, Wuhan University, Wuhan 430072, China.

[2] Changjiang River Scientific Research Institute, Wuhan 4300710, China.

Corresponding author: Zhiwei Li (lizw2003@whu.edu.cn)

Key Points:

- A new method of braided water body extraction improves accuracy of recognition
- The warming and wetting trend has led to the durative activation of braided rivers since 2000
- Intra-annual channel migration intensity differently responds to the increase of water and sediment flux in nine braided rivers

Abstract

With the rising air temperature and precipitation, water and sediment flux in the Source Region of the Yangtze River have increased significantly since 2000. Nonetheless, the response of braided river morphology to climate-driven water and sediment flux change is still unknown. Water bodies of nine large braided rivers from 1990 to 2020 were extracted based on Google Earth Engine platform, and impacts of climate change on activation indices of braided river morphology were quantified. The main results are presented that a new method of braided water body extraction by combining Lowpath algorithm and Local Otsu algorithm is firstly proposed, which reduces 59% of the root mean squared error of braiding intensity in comparison with the Global Otsu method. The braiding intensity has a parabolic variation trend with the water area ratio, and the average sandbar area ratio has a negative power law trend with the water area ratio. Intra-annual channel migration intensity has an obvious temporal scale effect, which increases rapidly when the time span is less than 5 years. The warming and wetting trend led to vegetation cover increasing significantly. With the increase of runoff, water area of each braided reach has increased in both flood and non-flood season. Intra-annual channel migration intensity shows three different trends of increasing, weakening, and unchanged over time. The response of migration intensity to climate warming can be classified into three patterns in the SRYR as follows: sediment increase constrained pattern, sediment increase dominated pattern, and runoff increase dominated pattern.

1 Introduction

As the highest dynamic and unpredictable river pattern, braided river is a complex system of shallow multi-threaded channel which separated by irregular sandbars. Morphodynamic processes of braided river are intensified during flood period (Lu et al., 2022; Shampa and Ali, 2019). Moreover, owing to the intensive erosion and deposition of multi-threaded channel, riverbed configuration is rapidly adjusted (Li et al., 2020d; Lu et al., 2022; Shampa and Ali, 2019). These changes are related to the hydrodynamic conditions of river network, non-equilibrium sediment transport, local erosion and accretion, bifurcation, and confluence of branches. For instance, inundated sandbars in flood period are prone to be transversely or obliquely cut under the action of lateral hydraulic gradient between adjacent branches (Schuurman et al., 2018). Owing to the complexity and instability of this system, it is difficult to exactly predict the evolution processes of braided rivers by theoretical analysis or numerical model (Lu et al., 2022; Schuurman et al., 2018).

The Source Region of the Yangtze River (SRYR) is an aggregation region of many large braided rivers, with the maximum width of channel belt reaching 3 ~ 5 km (Li et al., 2020d). This concentrated distribution of large braided rivers is very rare on the Qinghai-Tibet Plateau (QTP), in the Asian High Mountains and even the global alluvial rivers (Ashmore, 2013; Surian and Fontana, 2017). The evolution processes of braided rivers in the SRYR are highly free from the interference of human activities. Hence this region is conducive to uncover fluvial process of braided rivers driven by climate warming on the QTP. Meanwhile, braided river is an important component of aquatic ecological environment in the SRYR, which is closely related to the diversity and integrity of the alpine aquatic and terrestrial ecosystems. Large braided rivers play an irreplaceable role in maintaining fragile ecological balance, protecting biodiversity, and resisting sandstorms. These braided rivers are of great significance to hydrological cycle and ecological security of the Three-River Source region and even the entire QTP.

In recent years, some studies on braided rivers in the QTP mainly focus on morphological characteristics of braided rivers and their response to changes in hydrological regime caused by upstream dam construction (Guo et al., 2023; Li et al., 2020d; Lu et al., 2022; Shampa and Ali, 2019; You et al., 2022). In the UlanBuh Desert reach of the Upper Yellow River, the water and sediment flux gradually decrease and aeolian activities were weakened after 1990, result in the weakened lateral migration ability of braided channel (Li et al., 2018). In the middle and lower Lhasa River in the southern QTP, after upstream dam construction, braided channel generally transforms into lower complexity (You et al., 2022). The previous study of braided rivers in the SRYR demonstrated that braiding intensity and valley width are the two main parameters affecting the morphological characteristics (Li et al., 2020d). The branches after flood peak were eroded deeper, and furthermore the braiding intensity was greater after the flood than that before the flood (Lu et al., 2022). In the Maqu Reach in the Source Region of Yellow River in the QTP defined as a transition state between anabranching river and braided river, displays the high stability due to its sufficient vegetation coverage (Guo et al., 2023). To sum up, previous studies on braided rivers in the QTP are mostly concentrated in a single channel reach, and fail to make full use of existing abundant remote sensing imagery to study morphological characteristics and evolution processes of braided rivers in response to climate warming.

With the rise of air temperature and precipitation, hydrological condition in the SRYR was significantly altered. The water and sediment flux have shown a significant increasing trend in recent years (Deng et al., 2022; Li et al., 2020a; Luo et al., 2020; Yao, 2019), at an annual increasing rate of 1.4% and 5.9%, respectively (Li et al., 2020a). The main reason for the increase of runoff is the increase of precipitation (Luo et al., 2020). Meanwhile, the melting of glaciers and snow cover, retreating of permafrost, prolonged thawing period that caused by climate warming also promote the runoff (Allen et al., 2019; Qi et al., 2015; Sakai and Fujita, 2017; Wang et al., 2009; Zhang et al., 2008). Furthermore, climate warming accelerates the melting of glaciers and permafrost, which is the main reason for the substantial increase of sediment flux in recent 30 years (Li et al., 2020a). The synchronous increases of water and sediment flux will inevitably lead to more drastic riverbed evolution of braided rivers (Ashmore, 2013; Shampa and Ali, 2019; You et al., 2022), which threaten the safety of railways, trans-river bridges and other infrastructures. Meanwhile, the vegetation coverage in the SRYR also shows an increasing trend (Ji et al., 2021; Li et al., 2021c; Wang et al., 2022), which was supposed to limit the sediment production capacity and enhance riverbed resistance. Water and sediment conditions are the dominant driving forces of multi-scale morphological evolution of braided rivers, their impact degrees and activation patterns on braided rivers at the SRYR are an unsolved scientific problem.

The main aim of this study is to elucidate the morphological characteristics and activation of 9 large braided rivers in the SRYR in response to climate-driven water and sediment flux change over the last 30 years. This study proposes a new remotely sensing interpretation method of water body extraction for the morphological characteristics of braided rivers. Firstly, based on Google Earth Engine (GEE) platform, multi-source remote sensing images (Landsat 5/7/8 and Sentinel-2) were used for water body extraction of 9 selected braided reaches. The morphological characteristic parameters (i.e., channel count index, water area ratio, average sandbar area ratio) were calculated, and their variation were studied. Secondly, Google Earth, Landsat 7, and Sentinel-2 images were used to analyze the erosion rate of river bankline for the past 20 years. Finally, the variation trend of the intra-annual channel migration intensity of each braided reach from 1990 to 2020 was quantified. The response of migration intensity to climate

warming was analyzed in combination with the change of vegetation abundance, runoff, and sediment fluxes. The flow chart of the methodology proposed in this study is presented in Fig. S1.

2 Materials and Methods

2.1 Study area

The Source Region of the Yangtze River (SRYR) (32° 30' ~ 35° 35' N, 90° 43' ~ 96° 45' E) is located in the hinterland of the Qinghai-Tibet Plateau (QTP), with an average elevation of 4,780 m a. s. l. It is a relatively gentle and eastward sloping wave-like plain, which is not only a primary part of the Source Region of the Three Rivers (43.6% of the total area), but also an important water conservation area in the Upper Yangtze River (Changjiang River). The SRYR consists of the mainstream Tongtian River and the three main tributaries of Tuotuo, Dangqu, and Chumaer Rivers, with a catchment area of 138,200 km^2 (Fig. 1). The annual runoff is 12.26 billion m^3, accounting for about 1.3% of the total runoff of the Yangtze River. The mean annual air temperature in the SRYR ranges from -1.7 ℃ to 5.5 ℃, and the annual rainfall ranges from 200 mm to 550 mm. In terms of climate, the SRYR is located in the Naqu Goluo subhumid region and Qiangtang semi-arid region, which belong to the sub-cold zone of the QTP, and show a general trend of high temperature in the southeast and low in the northwest. Air temperature is characterized by small intra-annual temperature difference and large diurnal temperature variation, with long winter and short summer. The main land cover types in the SRYR are grassland (53%) and bare land (43%) (Yan et al., 2020). The SRYR has the most concentrated distribution of 753 glaciers on the high mountains at the edge of the river basin, with a total area of 1,276 km^2, accounting for 1.0% of the SRYR area. The runoff of glacier meltwater only accounts for 9.2% of the annual runoff of the SRYR (Yang et al., 2003; Yao et al., 2022).

The river network system in the SRYR originates from glacier and snow-capped mountains, with large gradient, dramatic discharge variation, underlying permafrost and large amount of coarse sand. Therefore, the dominant alluvial river type is gravel-sand braided channel (Li et al., 2016, 2020d, 2020e; Yu et al., 2014). Large braided rivers are mainly distributed in the main and tributary systems such as Tuotuo, Chumaer, Buqu, and Tongtian Rivers. Unstable and unvegetated gravel or sand bars form the riverbed with extremely fragmented channel morphology.

The impacts of climate warming on the morphological characteristics and activation of braided rivers were studied on selected 9 braided reaches wider than 1 km. Reaches are located in Tuotuo, Dangqu, Chumaer, Buqu, Beilu, Gaerqu Rivers, and the upper, middle and lower reaches of Tongtian River (termed as *TTR_S*, *TTR_M*, *TTR_E*) (Fig. 1a). Among them, the Dangqu, Buqu, and Gaerqu Reaches come from the Dangqu River Basin with dense wetlands, marsh area, better hydrothermal conditions (Fig. 5a, b) and rich vegetation cover (Fig. S16a, c). The hydrothermal condition of the Chumaer and Beilu River Basins is poor (Fig. 5a, b) with sparse vegetation cover (Fig. S16a, c) and loose soil. The land cover type in the Tuotuo River Basin is mainly alpine grassland with poor hydrothermal conditions (Fig. 5a, b). Reaches of *TTR_S*, *TTR_M* and *TTR_E* are restricted by valley confinement, as shown in Fig. 5a, b. The *Test* Reach (Fig. 1b) which is located in the *TTR_E* Reach, is used to evaluate the accuracy of the new Local Otsu + Lowpath water extraction method proposed in this study (Fig. 4c, d). The catchment area of each reach is shown in Fig. 1a for calculating the catchment mean annual *NDVI* level (Fig. S16).

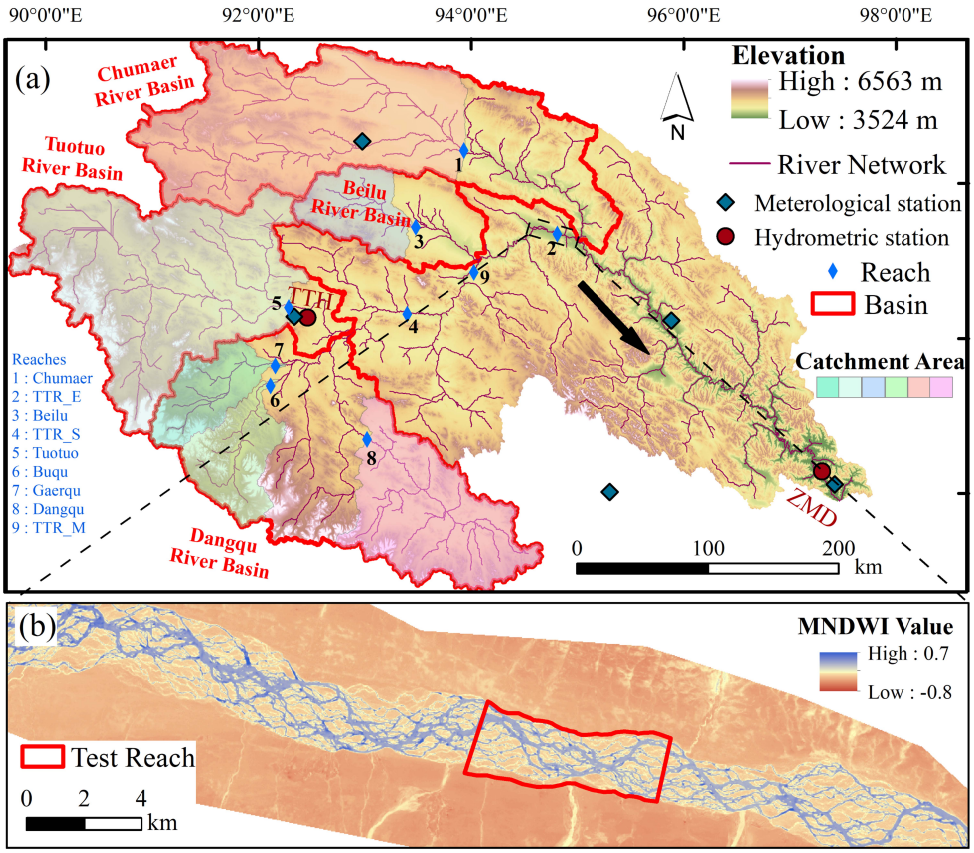

Figure 1. Location of braided reaches in the SRYR. (a) Study reach of each braided river and its catchment area, the sub-basins. The study reaches were named according to the name of the river, in which the upper, middle and lower reaches of the Tongtian River were named *TTR_S*, *TTR_M* and *TTR_E* respectively. In addition to the main stream of the Tongtian River, the rest of the study reaches are distributed in four sub-basins, namely, Dangqu, Tuotuo, Beilu, and Chumaer River Basins. (b) The *Test* Reach of *TTR_E* Reach was used to evaluate the accuracy of the new Local Otsu + Lowpath method for extracting braided river water bodies.

2.2 Methods

Landsat 5/7/8 and Sentinel-2 images from 1988 to 2020 were used for braided river interpretation. With high temporal resolution and comprehensive spatial coverage, remote sensing image interpretation has become an important method to study the evolution of rivers around the world, especially in remote areas (poor accessibility) (Deng et al., 2022; Huang et al., 2021) such as the SRYR (high altitude, harsh weather, and inconvenient transportation) (Deng et al., 2022; Gao et al., 2022; Li et al., 2020d). The Landsat imageries have a spatial resolution of 30 m and a revisit period of 16 days. Sentinel-2 imagery consists of images of Sentinel-2A and Sentinel-2B satellites, which was launched in June 2015 and March 2017, respectively, with a revisit period of 5 days. In the SRYR, Landsat 5/7/8 imageries were available from 1988 to present, and Sentinel-2 imagery were valid from 2016 to present. Snow, ice, and cloud may cover the river channel, negatively affecting the recognition of braided river morphology. The freezing period is from October to May, during which the braided river is partially or completely

covered with snow and ice. Therefore, from 1988 to 2020, cloud-free images between May and October were selected for further research (Table 1).

Landsat 5/7/8 and Sentinel-2 imageries used in this study were all from the Google Earth Engine (GEE) platform (Gorelick et al., 2017). Compared with traditional image processing tools (such as ArcGIS, ENVI, Matlab) using a single computer, GEE platform has millions of servers worldwide. With the most advanced cloud computing and cloud storage capacity, GEE is enabling more efficient online image processing. Owing to the high efficiency and data availability, GEE can be used to extract water bodies at large spatiotemporal scales (Deng et al., 2022; Huang et al., 2021; Li et al., 2020b). Based on GEE platform, Landsat 5/7/8 and Sentinel-2 imageries were filtered and clipped, then *MNDWI* (Xu, 2006) and *NDVI* (Carlson and Ripley, 1997) index were calculated. *MNDWI* images were downloaded, and Sentinel-2 images were resampling to 30 m spatial resolution.

The meteorological data used in this paper are from the daily values of China surface data (SURF_CLI_CHN_MUL_DAY V3.0) and ERA5 data sets. Air temperature and precipitation data from four stations within the SRYR and the Zado meteorological station outside the source region (Fig. 1a) during 1957 ~ 2020 were used to calculate the interannual values of precipitation and average air temperature. The spatial distribution of air temperature and precipitation during 1979 to 2020 (Fig. 5a, b) was calculated in GEE, based on monthly mean air temperature and monthly precipitation data obtained from ERA5 dataset (Dee et al., 2011).

Long-term hydrological data only come from Tuotuohe (TTH) and Zhimenda (ZMD) Hydrological Stations. TTH Station controls the Tuotuo River Basin, while ZMD Station controls the whole SRYR (Fig. 1). The hydrological data of the TTH Station include daily discharge data from 1958 to 2018, which can reflect the runoff condition of the Tuotuo Reach. The data of annual water and sediment discharge at the ZMD Station were obtained from Qinghai Hydrological Bureau (1987 ~ 2014) and Bulletin of China River Sediment (2000 ~ 2020). The daily runoff data of ZMD Station in 2018 are used to indirectly reflect the flow condition of *TTR_S*, *TTR_M*, and *TTR_E* Reaches.

Table 1. Selection of remote sensing images for each reach

Reach	$L \times W$ (m)	Landsat + Sentinel			Google Earth (Landsat 7 + Sentinel-2)			
					T_1		T_2	
		Total pics	Resolution /m	Process Time (per pic) /s	Year	Resolution/m	Year	Resolution /m
Beilu	5600×1092	85	30	4.24	2010	0.30	2020	0.30
Buqu	8400×1371	152	30	5.53	2005	0.30	2020	0.30
Chumaer	7400×1215	95	30	5.68	2007	0.30	2020	0.30
Dangqu	9600×1333	95	30	6.32	2000	15 (Landsat 7)	2020	10 (Sentinel-2)
Gaerqu	8000×888	184	30	5.22	2003	0.30	2020	0.30
TTR_E	33000×2740	116	30	19.78	2012	0.30	2020	0.30
TTR_M	16200×2771	178	30	9.87	2000	15 (Landsat 7)	2020	10 (Sentinel-2)
TTR_S	11000×2763	108	30	7.83	2010	0.30	2020	0.30
Tuotuo	18600×1010	245	30	9.04	2003	0.30	2020	0.30

Note: L is the reach length, W is the average reach width.

2.2.1 Analysis of meteorological and hydrological trends

The Mann-Kendall trend analysis (Kendall, 1975; Mann, 1945) and Sen-Slope (Sen, 1968) were used to analyze the significance level and variation trend of meteorological and hydrological data (air temperature, precipitation, runoff, and sediment discharge) over time. As a nonparametric method, Sen-Slope can be used to calculate the trend of univariate time series. This method is insensitive to outliers and is widely used in trend analysis of hydrometeorological data (Huang et al., 2021; Panda and Sahu, 2019). Mann-Kendall trend analysis was applied to analyze the inter-and intra-annual variation of meteorological and hydrological data during 1957 ~ 2020.

2.2.2 The characterization of vegetation abundance for different spatial scale

As the main part of terrestrial ecosystem, plants play an important role in regulating regional hydrological processes. Normalized vegetation index (*NDVI*), as an indicator of plant growth status and vegetation spatial coverage, is linearly positively correlated with vegetation density (Carlson and Ripley, 1997).

$$NDVI = (NIR - R)/(NIR + R) \quad (1)$$

where *NIR* is the near-infrared band, corresponding to B4 in Landsat 5/7, B5 in Landsat 8, and B8 in Sentinel-2. *R* is the red band, corresponding to B3 in Landsat 5/7 and B4 in Landsat 8 and Sentinel-2.

Owing to the influence of cloud, rain, and snow, remote sensing images are manifested as low value noise in *NDVI* image. To eliminate such influence, the maximum value composite method (MVC) is usually used to take the maximum value in a certain period as the pixel value. The *NDVI* image set was calculated based on Landsat 5/7/8 remote sensing images. The MVC composite method was used to calculate the variation of *NDVI* values in each river basin, river channel (Fig. S16c, d), and the catchment area of each reach (Fig. 1a) (Table S5, Fig. 16) over time. Based on the inter-annual *NDVI* image set synthesized by MVC method (*MVC-NDVI* image), the Sen-Slope (Sen, 1968) was used to calculate the increase rate of annual *NDVI* value at each pixel (Fig. S16b), reflecting the spatial difference of *NDVI* value increase. All calculations of *NDVI* are performed in the GEE platform.

The *MVC-NDVI* image is affected not only by growth cycle of vegetation on sandbars, cloud cover, but also by the temporal resolution of imageries, and even flood events when focusing channels. Therefore, the maximum value composite within a single year may not reflect the highest vegetation abundance, and a three-year period composition is adopted (Fig. S16c, d). In the composition of *MVC-NDVI* image of river channel, sandbar vegetation tends to have low value, which is comparable to the low value of clouds, could mask process need to be done in advance to eliminate such influence. Furthermore, in order to reduce the disturbance of vegetation outside the river bank, a -100 m buffer was set for the studied channel region.

2.2.3 Calculation of morphological indices in braided river

Based on the extracted river water body, reach-scale morphological indices were calculated. Namely, branch count index B_{T3} (Ashmore, 2013; Egozi and Ashmore, 2008), active water area ratio R_W (Li et al., 2020d), and average sandbar area ratio $\overline{R_b}$.

$$R_W = A_W/A \quad (2)$$

where A_W is the water area of the reach, and A is the channel area of the reach by visual interpretation (channel is the area that consists of channel branches and associated bars (Limaye,

2020)). The active water area ratio R_W (Li et al., 2020d) can reflect the proportion of braided channel water area under different water stage.

$$B_{T3} = \Sigma N_i / n \tag{3}$$

where n is the number of cross sections within the reach, and N_i is the number of branches on i-th cross section. B_{T3} is widely used to characterize the braiding intensity of braided river because of its easy calculation and clarity (Egozi and Ashmore, 2008; Li et al., 2020d; Lu et al., 2022). In general, n cross sections with a certain step length are set along the central line of the river, and cross-section was set with 200 m interval in this study. In this study, 200 m interval is good for the 10 times reach length to reduce systematic error (Egozi and Ashmore, 2008).

$$\overline{R_b} = \frac{\Sigma A_{bar}^{i}}{n_{bar} A} \tag{3}$$

where $\underline{n_{bar}}$ is the number of sandbars within the reach, and A_{bar}^{i} is the area of the i-th individual sandbar. Average sandbar area ratio $\overline{R_b}$ represents the average size of all bars.

Li et al. (2020d) found the parabolic relationship between B_{T3} and R_W. Under different R_W, B_{T3} can be represented by Eq. (5).

$$B_{T3}(R_W) = a(R_W - R_W^*)^2 + B_{T3peak} \tag{4}$$

where B_{T3peak} is the maximum value of the fitted parabola, R_W^* is the corresponding water area ratio, and a is the quadratic term coefficient.

2.2.4 A new extraction method of braided river water body

Water body is usually extracted, using specific algorithms or visual interpretation, based on index image (such as *MNDWI*) calculated from remote sensing image. Water index can be used in various ways, such as multi-index combination (Monegaglia et al., 2018), optimal index selecting by multi-index comparison (Talukdar and Pal, 2019; Worden and de Beurs, 2020), or use water indexes by priority (Deng et al., 2022; Huang et al., 2021). It is appropriate to use *MNDWI* (Eq. (6)) to calculate water index for water extraction of braided river (Singh et al., 2015; Xu, 2006).

$$MNDWI = (G - MIR)/(G + MIR) \tag{5}$$

where *MIR* is in the mid-infrared band, corresponding to B5 in Landsat 5/7, B6 in Landsat 8, and B11 in Sentinel-2. *G* is the green band, corresponding to B2 in Landsat 5/7 and B3 in Landsat 8 and Sentinel-2. The calculation of *MNDWI* was carried out in the GEE platform.

Water extraction algorithms mainly consist of threshold segmentation method (Pekel et al., 2016; Singh et al., 2015; Xu, 2006) and image recognition method (Zhu et al., 2015). In river water extraction, the Global Otsu method (Otsu, 1979) was mostly used to segment index image (Deng et al., 2022; Monegaglia et al., 2018). Global Otsu method (Otsu, 1979) calculates the histogram of pixel value distribution and automatically calculates a threshold value to maximize the inter-class variance of the two types of pixels divided by the threshold value. The Global Otsu method is a non-parametric and non-supervised method, of which the threshold value will be affected by delimited range of the studied area. There is a certain drawback in water body extraction of braided river using the Global Otsu method.

The use of a single threshold method (such as Global Otsu method) can underestimate the complexity of the extracted water body of braided river. A reach in the Tuotuo River was selected to analyze the transverse distribution characteristics of the *MNDWI* value of the braided river (Fig. 2). The red dotted line is the global Otsu threshold calculated based on *MNDWI*

image. Each peak in the profile map corresponds to a branch (P1 ~ P10). As shown in the profile, the *MNDWI* peak value of the main branch is significantly higher than that of the secondary branch. When the Global Otsu threshold is used, except for P3, P4, P5, P7 and P8, the peak values of secondary branches are lower than the Global Otsu threshold and hence cannot be identified. Even if the threshold is lowered, for example, by changing the threshold to -0.1, branches P1, P2, P6, P7, P8, P9 can be identified, but P3, P4, and P5 will be recognized as one branch. A single threshold partition cannot always identify all branches simultaneously and further underestimates the complexity.

According to our analysis, global threshold is not suitable for the segmentation of braided rivers. The main reason is ascribed to the spatial resolution (30 m) of Landsat remote sensing image relatively lower than the width of braided river branches. The *MNDWI* value of the edge pixel, which contains both parts of water and nan-water area, will be lower than the value of pixel of 100% water. Hence, the peak value of *MNDWI* will decrease in many branches of braided river whose width is close to or slightly less than the spatial resolution of remote sensing image. Although the peak value of the branch is significantly higher than that of the surrounding sandbar area by visual estimation, the peak value of the branch is also significantly lower than that of the mainstream. This suggests that water body cannot be divided by a single threshold method, regardless of whether the threshold is defined by custom or by algorithm, unless a higher resolution image is used. For the issue mentioned above, researchers generally extract water body with a single threshold value and then manually correct the errors (Li et al., 2020d). For a long braided reach, however, this manual method will result in a huge workload.

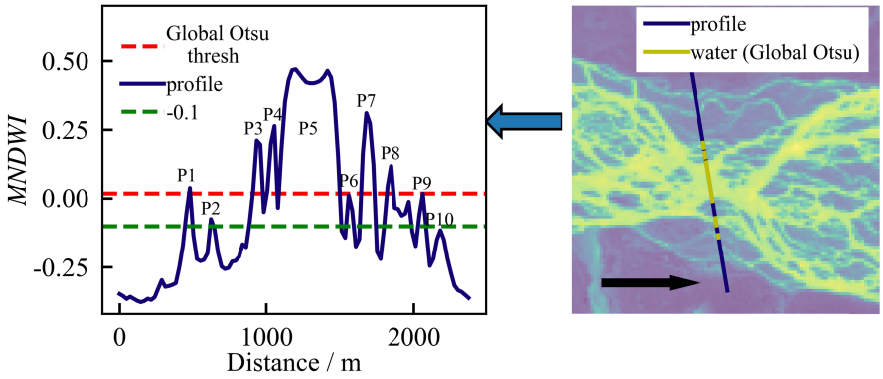

Figure 2. Identification of braided river branches by global threshold segmentation method.

This study adopted the combination method of Lowpath algorithm and Local Otsu algorithm to extract water body of braided river. Local Otsu Method (Farrahi Moghaddam and Cheriet, 2012, 2010; Nicolaou et al., 2014) takes each pixel of the image as the center, considers pixels in a certain range around the central pixel according to a morphological mask (convolution kernel). We used the Otsu method to calculate the threshold of each pixel. Each pixel of the image has a different threshold. Here, a circular convolution kernel with radius 5 was used to calculate the Local Otsu threshold, which was completed by Python's Skimage library (Lynch, 2018). The calculation results of the Local Otsu method are not affected by the size of the study area, and pixels with higher local values can be extracted (Fig. 3b). The Lowpath algorithm (Hiatt et al., 2020) was used to calculate the topological structure of braided river by identifying saddle points and local minimum points in DEM (Digital Elevation Model) and calculating the lowest path between them. Meanwhile, all links were graded according with δ value (the volume between two adjacent links) in this algorithm. Lowpath was originally designed to be used in DEM (Hiatt

et al., 2020; Sonke et al., 2022). DEM shows a low value at the branch (low elevation), while *MNDWI* shows a high value at the branch (Fig. 2). This commonality makes the Lowpath also applicable to *MNDWI* image. Here we transform the data type of the water image into uint-8 datatype (0 ~ 255 integer) and extracts all links with the $\delta > 50000$ (Fig. 3c). The Local Otsu method was used to calculate the water body, and the Lowpath was used to calculate the topological structure. The union of the two methods can supplement the small branches in braided rivers whose widths are smaller than the pixel resolution (30 m), which may not be fully recognized in the Local Otsu method (Fig. 3d).

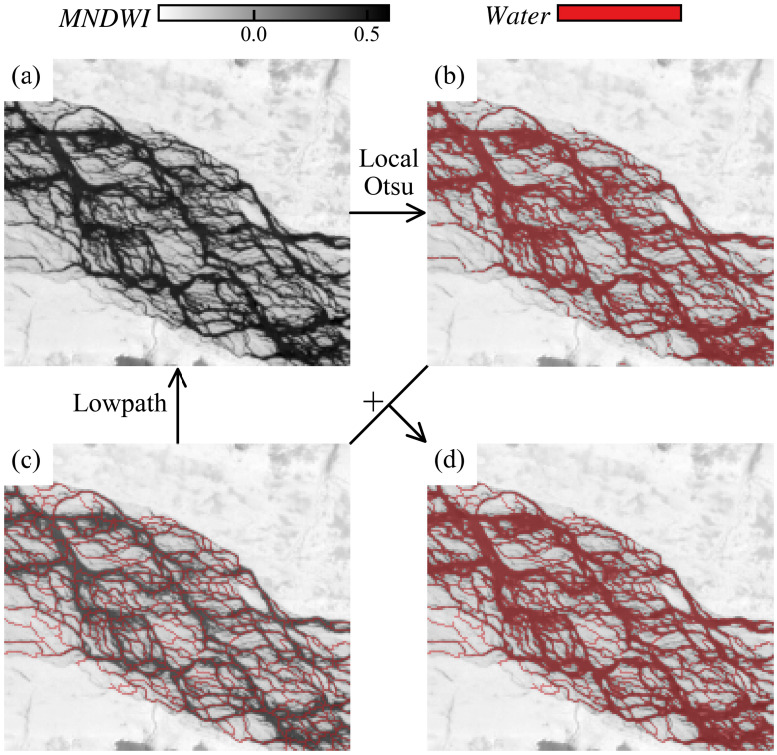

Figure 3. Water extraction for braided river with Local Otsu + Lowpath method. (a) *MNDWI* image of braided river, (b) water body calculated by Local Otsu method, and (c) water body calculated by Lowpath method, (d) water extraction results of Local Otsu + Lowpath method.

Compared with the Global Otsu method, the Local Otsu + Lowpath method can better extract water body of braided river and more accurately estimate the complexity of braided river morphology. To evaluate the accuracy difference between the new method and the traditional method (Global Otsu), images of *Test* reach (Fig. 1b), a sub-reach of *TTR_E* reach, were selected from the 2018 (Table S1). The water body is extracted by using the Local Otsu + Lowpath method and Global Otsu method, B_{T3} and R_W are calculated respectively and the real B_{T3} is calculated by the visual interpretation. A cross-section was set at an interval of 200 m. It can be seen from Fig. 4c that the braiding intensity B_{T3} calculated by the new method is close to the true value, with a root mean squared error (RMSE) of 1.37. Meanwhile, the B_{T3} calculated by the Global Otsu method has a RMSE of 3.32. Compared with the Local Otsu + Lowpath method, the R_W calculated by Global Otsu method is larger (Fig. 4d). This is because, when the Global Otsu method was applied, many shallow and narrow branches will not be recognized. Some parts of sandbars around wide and deep branches will be misidentified as water bodies, resulting in underestimated complexity and connectivity, and overestimated water area (Fig. 4b). Meanwhile,

the new method proposed in this study (Fig. 4a) can identify more small branches of braided rivers and more accurately reflect the connectivity, complexity, and water area of braided rivers. Water segmentation was based on *MNDWI* images downloaded from the GEE platform. Using the Local Otsu + Lowpath method, the time requirement of water segmentation per image of each reach ranges from 3.87 to 19.78 s, and a wider and longer river will increase the calculation time (Table 1).

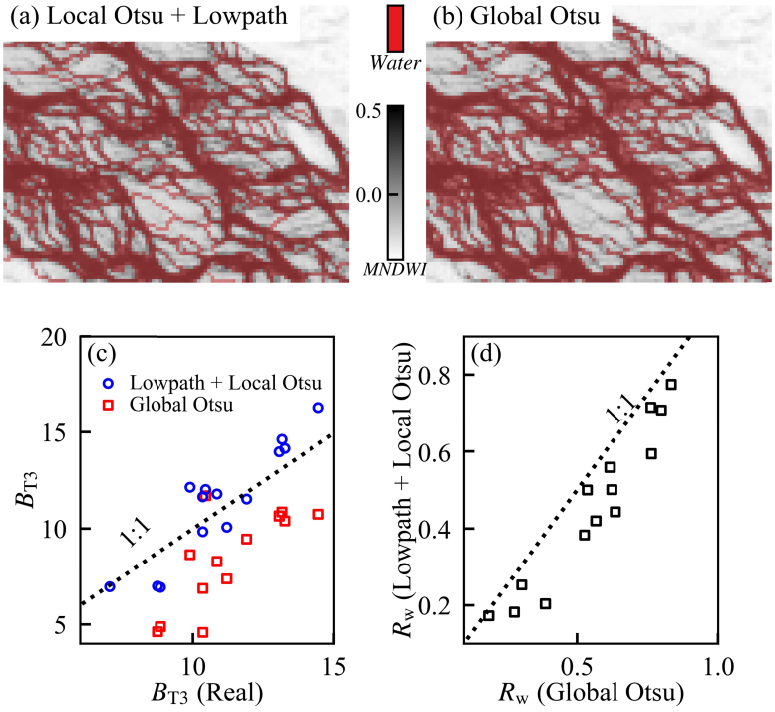

Figure 4. Comparison of water extraction results between the Local Otsu + Lowpath method and Global Otsu method. (a) Comparison of water extraction results of the Local Otsu + Lowpath method (b) Global Otsu method. (c) Comparison of braiding intensity B_{T3} extracted by the Local Otsu + Lowpath method and Global Otsu method with B_{T3} (Real) value interpreted by the visual interpretation; (d) Comparison of water area ratio R_W between the two methods.

2.2.5 The expression of interannual change of braided channel water area

The river discharge changes rapidly over time, and the acquisition of Landsat remote sensing images is limited by time resolution (16 d) and cloud cover. Hence it is difficult to fully reflect the inter-annual variation of water area ratio (R_W) using remote sensing images. Therefore, the decadal variation of R_W in flood season (July and August) and non-flood season (May to June, September to October) was calculated to analyze the change of water area over time. The median value of R_W ($\widetilde{R_W}$) in flood season from 1990 to 2020 was used to reflect the inundation chance of the reach (Fig. 16).

2.2.6 Calculation method of lateral expansion of braided channel

Based on Google Earth submeter-level images and Landsat 7 and Sentinel-2 images, the expansion rate of the river channel is calculated. The M_R calculation method of the multi-year average expansion rate of the river channel is shown in Eq. (7).

$$M_R = \frac{A_{Chan}^{(T_2)} - A_{Chan}^{(T_1)}}{(T_2 - T_1)L} \tag{6}$$

where $A_{Chan}^{(T_1)}$ and $A_{Chan}^{(T_2)}$ are the river channel area (same as in Eq. (2)) of earlier and later images respectively; T_1 and T_2 are the years of the earlier and later images respectively; L is the reach length. In ArcGIS and Google Earth, the river boundary of two different periods was described by visual interpretation, and $A_{Chan}^{(T_2)}$ and $A_{Chan}^{(T_1)}$ were calculated. M_R could then be obtained by dividing the reach length L and the number of separated years T_2-T_1.

To calculate the channel area, the visual interpretation of river channel bank needs to be done. The submeter image of Google Earth has a spatial resolution of 0.3 m and can be used to accurately identify riverbanks. Google Earth submeter images are not available in some of the studied reaches (i.e., *TTR_M* and Dangqu River Reaches), thus the Landsat 7 and Sentinel-2 images are used as alternatives. To improve the accuracy of riverbank identification, panchromatic band (15 m resolution) of Landsat 7 was used for panchromatic sharpening of its multi-spectral band, of which the spatial resolution was sharpened to 15 m. Landsat 7 images after panchromatic sharpening (15 m resolution) in 2000 and Sentinel-2 images (10 m resolution) in 2020 were selected for the visual interpretation of riverbank. The specific image selection of each reach is shown in Table 1. All the later (T_2) images of the reach were shot in 2020, while the early (T_1) images were shot between 2000 and 2012.

In the calculation procedure of M_R, it is necessary to consider the mixed pixel error. When calculating M_R using Eq. (7), the visual interpretation of riverbank is conducted to compute the area of river channel. The edge is the pixel that passed by visually interpreted bank line, and the spatial bias between interpreted bank line and the true bank line is called by the mixed pixel error. The calculation method of the mixed pixel error of M_R is derived as follows.

There are three assumptions needed to conduct the error analysis below. (i) The deviation between the visually interpreted riverbank line and the real riverbank line is within 1 pixel, that is, pixels passed by the hand-drawn riverbank line and the real riverbank line are basically identical. (ii) The proportion of riverbed in these pixels is uniformly distributed between 0 and 1 (Rowland et al., 2016). (iii) The visually interpreted bank line is close to the center of edge pixel.

$$A_{Chan} = A_{Bank}^{(l)} + A_{Bank}^{(r)} + A_{Inside} \tag{7}$$

According to Eq. (8), the area of the river channel A_{Chan} determined by visual interpretation includes the real riverbed area inside and at the edge (left bank $A_{Bank}^{(l)}$, right bank $A_{Bank}^{(r)}$) of the channel. The real values of $A_{Bank}^{(l)}$, $A_{Bank}^{(r)}$ are unknow. Mixed pixel errors are produced when replacing $A_{Bank}^{(l)}$ and $A_{Bank}^{(r)}$ with visually interpreted riverbed area at the edge of channel $A_{Bank}^{(l)\prime}$ and $A_{Bank}^{(r)\prime}$. The calculation method of the mixed pixel error on the left bank and right bank is the same. The left bank is taken here as an example to illustrate the estimation methods of the mixed pixel error.

$$A_{Bank}^{(l)} = \frac{\Sigma X_i^{(l)}}{n_l} n_l A_p \tag{8}$$

$$A_{Bank}^{(l)\prime} \approx \mu n_l A_p \tag{9}$$

$$SE_X^{(l)} = \sigma / \sqrt{n_l} = \frac{1}{2\sqrt{3}\sqrt{n_l}} \tag{10}$$

419 According to Eq. (9), when the area of a single pixel is A_p, the number of pixels on the left
420 bank is n_l, and the proportion of riverbed in the i-th pixel on the left bank is $X_i^{(l)}$. The true
421 distribution of riverbank is unknown (that is, the distribution of $X_i^{(l)}$). Based on assumption (ii)
422 and by using the ensemble average μ of $X_i^{(l)}$, the real riverbed area of all edge pixels in left bank
423 can be estimated as $\mu n_l A_p$, which is basically identical to the visually interpreted riverbed area
424 $A_{Bank}^{(l)\prime}$ based on assumption (c) (since μ=0.5 in this case) (Eq. (10)). The mixed pixel error is
425 generated when replacing $\Sigma X_i^{(l)}/n_l$ with μ. Standard error $SE_X^{(l)}$ is used to estimate the deviation
426 between the sample mean $\Sigma X_i^{(l)}/n_l$ and the ensemble average μ (Eq. (11)).

427 $$e_{Bank}^{(l)} = SE_X^{(l)} n_l A_p = \frac{n_l A_p}{2\sqrt{3}\sqrt{n_l}} = \frac{\sqrt{n_l} A_p}{2\sqrt{3}} \tag{11}$$

428 According to Eq. (11), the calculation method of mixed pixel error $e_{Bank}^{(l)}$ is shown in Eq.
429 (12). The value of $e_{Bank}^{(l)}$ is determined by the number of riverbank edge pixels and the area of a
430 single pixel A_p.

431 $$e_{Chan} = \sqrt{{e_{Bank}^{(l)}}^2 + {e_{Bank}^{(r)}}^2} = \frac{A_p}{2\sqrt{3}}\sqrt{n_l + n_r} = \frac{A_p}{2\sqrt{3}}\sqrt{n} \tag{12}$$

432 $$e_{M_R} = \frac{\sqrt{{e_{Chan}^{(T_1)}}^2 + {e_{Chan}^{(T_2)}}^2}}{(T_2 - T_1)L} \tag{13}$$

433 where n is the total number of pixels on the left and right banks. Likewise, assuming that the
434 calculation of $A_{Chan}^{(T_1)}$ and $A_{Chan}^{(T_2)}$ of the channel area in the images of T_1 and T_2 are independent of
435 each other, the mixed pixel error of M_R (Eq. (7)) of the channel area change rate can be
436 calculated according to Eq. (14). According to the theory of error propagation, we assume that
437 the distribution of the riverbed area on the left and right banks is independent of each other. The
438 mixed pixel error e_{Chan} of A_{Chan} can be added in quadrature (Eq. (13)).
439 Visual interpretation of riverbank was done using Google Earth images and sharped Landsat
440 7 and Sentinel-2 images, with spatial resolutions of 0.3 m, 15 m and 10 m, respectively. Except
441 for *TTR_M* and Dangqu River Reaches, the rest of the reaches have Google Earth submeter
442 imagery (0.3 m resolution) to identify the riverbank lines, of which the mixed pixel error can be
443 ignored. The pixel size of image of *TTR_M* and Dangqu River Reaches is large (10 and 15 m),
444 whose e_{M_R} calculated by Eq. (14) are 0.0122 and 0.0157 m/a, accounting for only 0.8% and
445 10.8% of M_R value, respectively (Fig. 12). The results of the mixed pixel error are shown in
446 Table S2.
447

448 **2.2.7 Calculation of intra-annual river migration intensity**

449 In order to reflect the intra-annual channel migration intensity of branches in a certain period
450 of time, the reach-scale migration intensity index IM_I (Intra-annual Channel Migration Intensity)
451 was calculated based on Eq. (15).

452 $$IM_I = \frac{A_{acc} + A_{ero}}{A} \tag{14}$$

453 where A_{ero} and A_{acc} are the erosion and accretion area respectively, which can be obtained by
454 subtracting earlier water segmentation image from later water segmentation image, A is the
455 channel area. Since the morphological characteristics of braided rivers change significantly with

flow discharge (Lu et al., 2022), it is necessary to ensure that the daily discharge or water stage between the two images is similar to reduce the inundation error. Owing to the lack of enough hydrological data in different reaches, images with similar water area ratio R_W in each reach were selected to calculate the migration intensity, for specific image selection and corresponding water area ratio R_W, see Table S3. The value of R_W corresponding to the selected images is shown in Fig. S3. It should be noted that this method using Eq. (15) does not reflect the changes in the depth of the riverbed, but Eq. (15) can reflect both the transverse and longitudinal migration.

To study the variation of migration intensity IM_I over different temporal scale, a base year was selected from 1987 to 1990 for each braided reach, and the relative migration intensity IM_I of each subsequent year was calculated, as shown in Fig. 10. The R_W of water segmentation in all reach ranges from 0.18 to 0.22 (see Fig. S3b) to reduce the inundation error, for corresponding image selection, see Table S3b.

TTR_M and Tuotuo River Reaches were selected to analyze the relationship between the annual migration intensity IM_I and the annual discharge. To calculate the annual migration intensity IM_I, pairs of images should be selected before and after the flood season (July ~ August). For the *TTR_M* Reach, the time of image selection was before July 9 or after August 26 (see Table S3c). For the Tuotuo River Reach, except for one image shot on 2013/08/02, the other images were shot before May 27 or after August 22 (see Table S3d).

To study the temporal variation trend of the migration intensity, the multi-year average migration intensity $\overline{IM_I}$ for 3 ~ 5 years temporal scale in each reach was calculated using Eq. (16).

$$\overline{IM_I} = IM_I/\Delta T \tag{15}$$

where IM_I is defined by Eq. (15), ΔT is the number of years between the time when two images are taken. In Fig. 10, the migration intensity was control by the magnitudes of water and sediment flux of that year. The multi-year average migration intensity of 3 ~ 5 years $\overline{IM_I}$ can reflect the migration intensity level of each reach within a period, so it can be used to reflect the fluctuant trend of the migration intensity over time. The R_W difference among all image pairs ranges from -0.06 to 0.05 (see Fig. S3a). The migration intensity for the last 30 years was used to characterize the migration intensity level of each reach (Table S3e, Table S5, Fig. 16).

2.2.8 The estimation of relationship between water area ratio and daily discharge

To calculate the daily discharge Q at a given water area ratio R_W in *TTR_M* and Tuotuo Reaches, the R_W-Q relationship of *TTR_M* and Tuotuo River Reaches was established, respectively. The Tuotuo River Reach is valid of daily discharge data from 1988 to 1990, of which is only valid in 2018 in *TTR_M* Reach (ZMD Station) to indirectly reflect its flow regime, and can only use the limited images in 2018 for calculation. When establishing the R_W-Q relationship in the *TTR_M* Reach, in order to acquire R_W data as much as possible, images of whose channel was partially blocked by clouds is also taken into account. For the image partially covered by clouds, the water area in the reach can be calculated according to Eq. (17).

$$A_2 = A_2^*/A_1^* \times A_1 \tag{16}$$

where A_1 and A_1^* are the total and partial water areas in the river of the reference image respectively, and A_2^* is the partial water area in the image of which the river is covered partially by clouds. A global cloudless image is selected as the reference image, and its total water area A_1 is extracted. For the partially blocked image of the river, the water area A_2^* of the partially cloudless part is counted, and the water area A_1^* of the reference image in the same part of region

is counted. The total water area A_2 of the partially blocked image is calculated with Eq. (17). The calculation procedures are shown in Fig. S2. The reference image (Landsat 8, 2018/07/24) was selected, the information of other cloud-blocked images was shown in Table S4. The calculated R_W-Q relationship in the *TTR_M* Reach was shown in Fig. 14a. This method can be used because the water body segmentation (Local Otsu + Lowpath method) in the cloudless part, is free from the effect of cloud cover in other part (Fig. S2).

3 Results

3.1 Spatiotemporal variation of precipitation and air temperature

The precipitation and air temperature in the SRYR increase from northwest to southeast. The mean annual precipitation in the Dangqu, Beilu, Tuotuo, and Chumaer River Basins was 631.3, 533.5, 565.0, and 495.8 mm, respectively. The precipitation is more distributed in the lower Tongtian River and Dangqu River Basins. The mean annual precipitation in the Chumaer River Basin is less than 500 mm. The mean annual temperature of the Dangqu, Beilu, Tuotuo, and Chumaer River Basins are -5.37, -4.70, -6.65, and -6.63 ℃, respectively. The air temperature is lower in the Tanggula Mountain in the west, Hoh Xil Mountain in the northwest and the Sediri peak in the south. The air temperature is relatively higher along the Dangqu ~ Tongtian River valley.

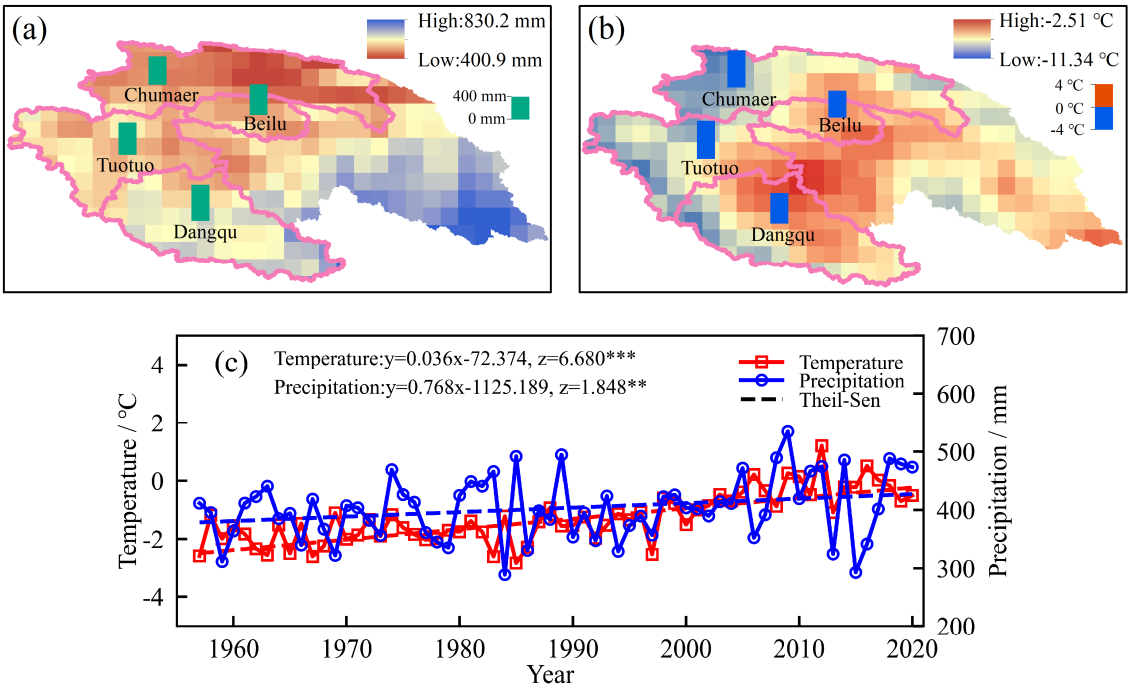

Figure 5. The meteorological change in the SRYR. Spatial distribution of (a) precipitation and (b) air temperature and (c) their variation trends of mean annual temperature and annual precipitation from 1957 to 2020 (mark **, *** denotes the significance level of p<0.05 and p<0.01).

From 1957 to 2020, the SRYR showed a warming and wetting trend, air temperature and precipitation increased significantly after 1990. The air temperature showed an overall increasing trend from 1957 to 2020, and the change rate was 0.36 ℃/10a (p=0.01). From 1960 to 2020, the decadal mean annual temperature is -1.96, -1.74, -1.77, -1.37, -0.57, and -0.10℃, and the inter-decadal temperature increase is 0.22, -0.03, 0.40, 0.80, and 0.47℃, respectively. Except for the

1970s and 1980s, where the temperature change was -0.03℃, the interdecadal temperature increment was more than 0.2 ℃ in any other decade, and the maximum temperature increment was 0.80 ℃ from 1990s to 2000s. From 1957 to 2020, the precipitation change rate was 7.7 mm/10a (p=0.05), showing a significant increasing trend. The decadal mean annual precipitation from 1960 to 2020 is 386.6, 390.0, 416.9, 381.7, 426.1, and 417.4 mm, and the inter-decadal precipitation increases of each decadal are 3.4, 26.9, -35.2, 44.3, and -8.7 mm, respectively. The mean annual precipitation was basically unchanged with slightly fluctuation from 1957 to 2000. The mean annual precipitation increased by 44.3 mm during 2000 ~ 2010 compared with 1990 ~ 2000, and decreased by -8.7 mm during 2010 ~ 2020 compared with 2000 ~ 2010, showing little change.

3.2 Variation trend of water and sediment flux

From 1957 to 2020, the water and sediment flux in the SRYR showed an increasing trend, both the water and sediment flux increased significantly after 2000. The annual runoff showed an overall increasing trend from 1957 to 2020, with a change rate of 0.703×10^9 m^3/10a (p=0.01). The decadal annual runoff in the five decadal periods was 12.891×10^9, 11.522×10^9, 14.312×10^9, 10.926×10^9, 14.899×10^9, and 16.015×10^9 m^3, respectively. The increase of mean annual runoff between each adjacent decadal period was -1.369×10^9, 2.790×10^9, -3.386×10^9, 3.973×10^9 and 1.116×10^9 m^3, respectively. The annual runoff fluctuated slightly and remained basically unchanged from 1957 to 2000, with the decadal mean annual runoff of 10.926 ~ 14.312×10^9 m^3. The mean annual runoff in 2000s increased by 36.36% compared with that in 1990s. In the 2010s it is a smaller increase of 7.49% in runoff compared to the 2000s. The decadal annual flux of suspended sediment was 9.056×10^9, 6.595×10^9, 8.768×10^9, 6.968×10^9, 7.762×10^9 and 11.931×10^9 kg from 1960s to 2010s, respectively. The sediment flux fluctuated slightly and remained basically unchanged from 1957 to 2000, with the decadal mean annual value ranging from 6.595 to 9.056×10^9 kg. The annual sediment flux began to increase after 2000. Compared with the 1990s, the decadal mean annual sediment flux increased by 11.39% in the 2000s, and furthermore increased by 53.71% in the 2010s compared to the 2000s. From 1957 to 2020, the change rate of sediment flux was 0.499×10^9 kg /10a (p=0.1 significant level), showing a significant increasing trend. In general, the water and sediment flux in the SRYR increased significantly after 2000 (Li et al., 2020a, 2023a).

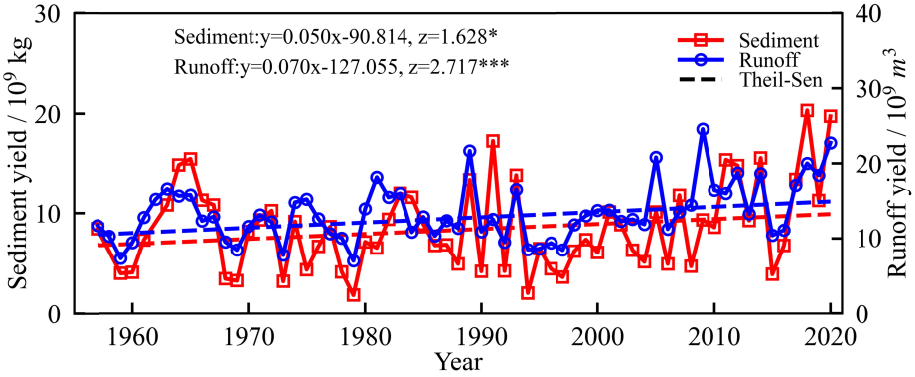

Figure 6. The hydrological variation in the SRYR from 1957 to 2020. (a) annual runoff and (b) annual sediment yield (mark *, *** denotes the significance level of p<0.10 and p<0.01).

3.3 Analysis of morphological characteristics of nine braided rivers

The braiding intensity increases first and then decreases with the increase of water area in a parabolic function, which is significantly related to the channel width. The analysis of 9 braided reaches in the SRYR show that the braiding intensity B_{T3} presents a parabolic trend with the increase of the ratio R_W of water area ratio (Fig. 7a), and the goodness of fit (R^2) ranges from 0.56 to 0.91. With the increase of R_W, the branches increase rapidly at first, when R_W increases to a certain extent, the adjacent branches merge and B_{T3} begins to decline. In Fig. 7b, there is a significant positive correlation between the average channel width W of each reach and the braiding intensity B_{T3peak} of the parabola peak (r=0.976, p=6.72·e^{-6}). It indicates that the channel width is an important factor affecting the complexity of braided channels (Li et al., 2020d).

Li et al. (2020d) studied the morphological characteristics of 6 braided reaches along the Tuotuo and Tongtian Rivers, and found the parabolic relationship between B_{T3} and R_W, with R^2=0.33 ~ 0.73 (Fig. S4), which is lower than that of this study (R^2=0.56 ~ 0.91), owing to the accurate extraction of braided river water bodies by the Local Otsu + Lowpath method. The R_W of the parabola fitting peak was termed as R_W^*. R_W^*=0.42 ~ 0.44 (Fig. S4) in the work of Li et al. (2020d), which is greater than R_W^*=0.29 ~ 0.40 as shown in Fig. 7a. This is because in the study of Li et al. (2020d), water extraction for *MNDWI* was divided by a single threshold, of which the R_W is generally larger than that of the Local Otsu + Lowpath method (Fig. 4d). Meanwhile, the centralized distribution of R_W indicates that the braided river in the SRYR have similar morphological characteristics. In the study by Li et al. (2020d), the B_{T3peak} of *TTR_E* Reach is 7.29 (Fig. S4e), while it is 12.15 in this study, showing an increase of 67%, due to the more complete identification by the Local Otsu + Lowpath method (Fig. 3, Fig. 4).

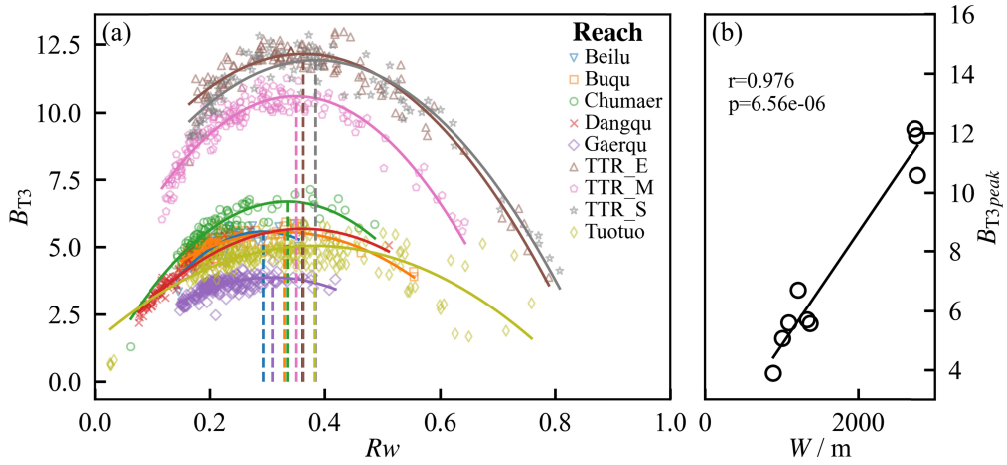

Figure 7. The variation rule of braiding intensity. (a) Variation of B_{T3} with R_W in the SRYR (b) Correlation between maximum braiding intensity B_{T3peak} and channel width W.

There is a significant negative power law correlation between average sandbar area and water area. With the increase of the water area ratio R_W, the average sandbar area ratio $\overline{R_b}$ shows a decreasing trend, which conforms to a negative power function in Fig. 8. With the increase of R_W, $\overline{R_b}$ decreases rapidly at first, due to the rapidly increasing amounts of sandbars caused by frequent cutting of overbank flow erosion. With the increase of discharge, R_W continues to increase, and the decline trend of $\overline{R_b}$ is slowed down. This is because the increase of R_W at this stage is mainly caused by the inundation of sandbars, which contributes little to the decrease of $\overline{R_b}$. The correlation between R_W and $\overline{R_b}$ is highly significant (p<0.001, |r|=0.79 ~ 0.99). This

negative power law relationship indicates the important morphological characteristics of sandbars in braided river.

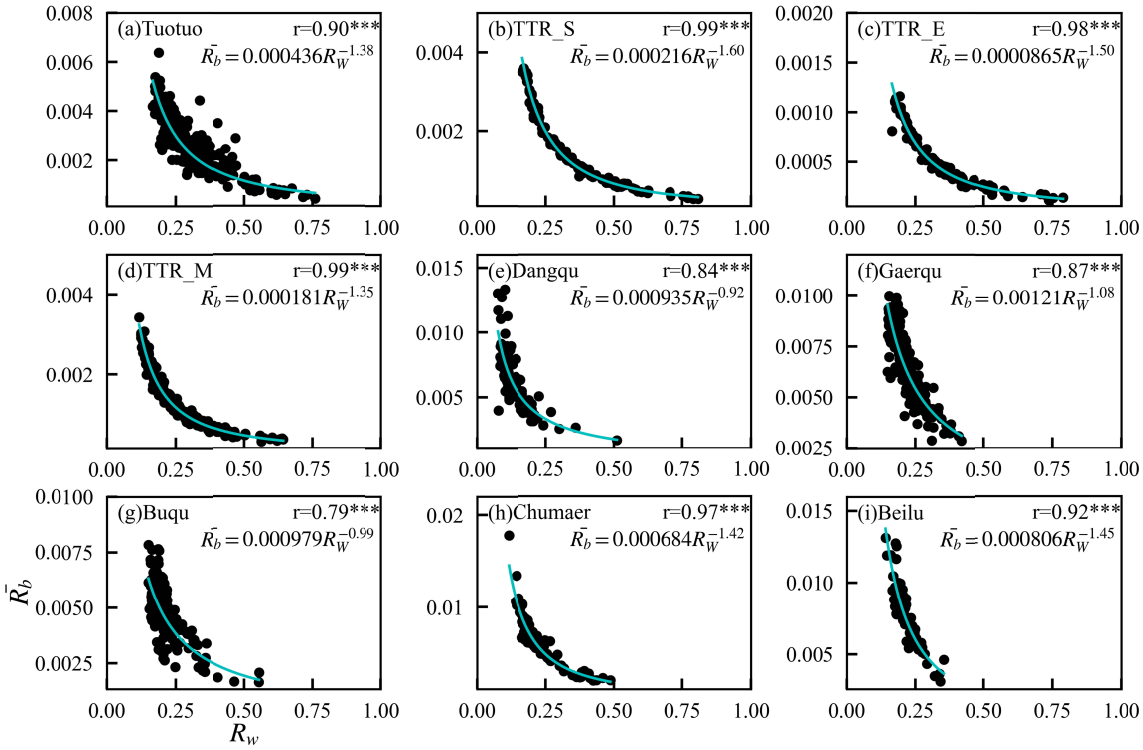

Figure 8. Correlation between average sandbar area ratio $\overline{R_b}$ and water area ratio R_W of each braided reach in the SRYR (mark *** denotes the significance level of p<0.001).

In Fig. 8, there is a negative power law relationship between the average sandbar area ratio $\overline{R_b}$ and the water area ratio R_W (Eq. (18)).

$$\overline{R_b} \propto 1/R_W^{\alpha} \tag{17}$$

where α is the opposite of the power exponent, $\alpha > 0$. The exponent α reflects the degree of fragmentation of the channel planform in the braided river. Under the same R_W increment, the greater the α, the greater the reduction of $\overline{R_b}$, which means that the sandbars are more fragmentated.

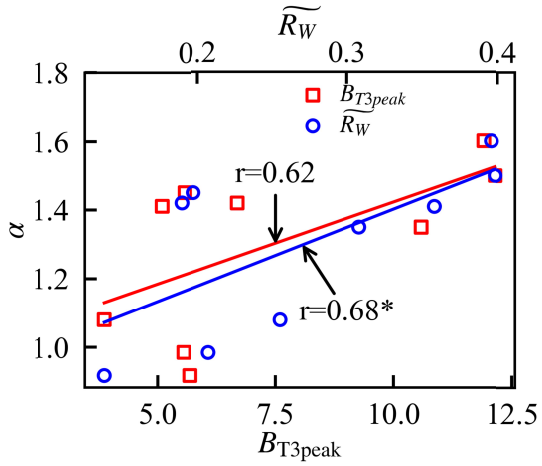

Figure 9. The correlation between index α, inundation chance $\widetilde{R_W}$ and *NDVI* level of river channel (mark * denotes the significance level of p<0.05).

The exponent α is positively correlated with B_{T3peak} and significantly positively correlated with inundation chance ($\widetilde{R_W}$). In Fig. 9, B_{T3peak} is significantly positively correlated with α (r=0.9, p=0.0731). This is because the higher braiding intensity is, the more fragmentated the sandbars in the channel, hence with the increase of the water area, $\overline{R_b}$ decreases more violently (which means higher α). The exponent α is also significantly positive correlated with the $\widetilde{R_W}$ (r=0.68, p<0.05), which means for braided channels with high inundation chance, sandbars are more likely to be cut during flood events (higher α). The exponent α can represent the degree of fragmentation of sandbars in braided reach.

With the increase of the temporal scale, the migration intensity of the braided river increases monotonously within 5 years, and then shows a stable fluctuation trend after 5 years. The variation rule of migration intensity IM_I over different temporal scale is shown in Fig. 10. The temporal scale was divided into three types based on the variation of IM_I. (a) Annual temporal scale (1 a): The magnitude of the annual migration intensity IM_I mainly depends on the annual runoff-sediment process. In high flow year, IM_I will be significantly higher than that in low flow year due to inundation action (Fig. 14a, Fig. 15a, b). (b) Medium temporal scale (2 ~ 5 a): IM_I shows a monotonically increasing trend within a 5-year temporal scale, which indicates an inherent inertia in the evolution process of braided river system. The direction and trend of riverbed erosion and deposition will maintain for a period. (c) Long temporal scale (greater than 5 a): After about 5 years, the increasing trend of IM_I slowed down, and the change trend tends to be flat and fluctuating, which is a manifestation of the instability of the braided river system (migration left and right). Consequently, the lateral migration of the branch is limited.

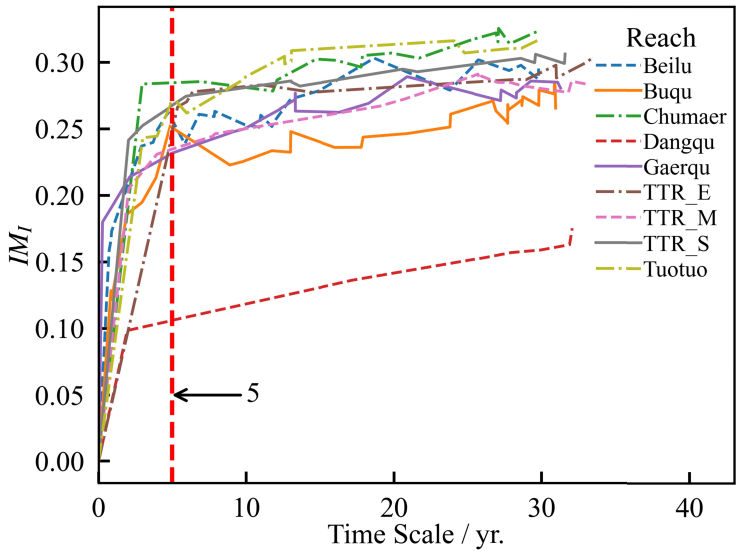

Figure 10. Relationship between migration intensity IM_I and corresponding temporal scale used for the computation of IM_I.

Over the longer temporal scale, the morphological characteristics of braided rivers change more dramatically. For any two images with identical R_W, the maximum value of IM_I calculated by Eq. (16) is $2R_W$ (meaning that there are no duplicate parts between the two water segments). The R_W of the selected images of each river segment ranges from 0.18 to 0.22, except for the Dangqu River Reach (maximum IM_I value 0.18, slightly lower than its R_W level). The maximum IM_I value of remaining reaches ranges from 0.29 to 0.33 (~1.5 times the R_W level), indicating that

the migration over a long temporal scale is very considerable. Compared with the base year, morphology in braided channel will change greatly after 5 years, so it is difficult to identify the trajectory of a single sandbar or branch. In this case, only the overall similarity of the plane morphology in braided channel can be observed.

The Dangqu River Reach ad the south source of the SRYR may be classified as anabranching river type according to our studies. The migration intensity in Dangqu River Reach is significantly lower than that of other reaches. The IM_I after 5 year is maintained between 0.10 and 0.18, and it shows a monotonically increasing trend with the increase of temporal scale, which indicates a long-term inertia of the migration direction (lack of instability). Therefore, even though the braiding intensity of the Dangqu River Reach is not low (B_{T3peak}=5.68), it is closer to the anabranching river type than to the braided river type from the viewpoint of braiding instability.

3.4 Impacts of water and sediment flux change on morphological characteristics of braided river

The Tuotuo and Tongtian Rivers Reaches are frequently inundated in flood season, while few inundation occurs in other reaches, even during flood season. For the Beilu, Buqu, Dangqu, Chumaer and Gaerqu River Reaches, the active water area ratio $\widetilde{R_W}$ were 0.197, 0.207, 0.138, 0.190, 0.255 in flood season, and 0.205, 0.182, 0.112, 0.212, 0.202 in non-flood season, respectively. Compared with non-flood season, the R_W in flood season shows little variation, ranging from -0.022 to 0.053 in $\widetilde{R_W}$. The $\widetilde{R_W}$ of these reaches in both flood and non-flood season are all smaller than R_W^*, which means low flooding chance. For the *TTR_E, TTR_M, TTR_S* and Tuotuo River Reaches, the $\widetilde{R_W}$ were 0.399, 0.308, 0.396 and 0.358 in flood season and 0.313, 0.207, 0.258 and 0.254 in non-flood season, respectively. Compared with non-flood season, the R_W in flood season increased with a relatively large amount, ranging from 0.076 to 0.138 in $\widetilde{R_W}$. The $\widetilde{R_W}$ of these reaches in flood season are close to or greater than R_W^*, while all less than R_W^* in non-flood season, which indicates high intra-annual flow variation (frequently flooding braidplain during flood season). High flow variation is conducive to the development of braided channels (Ashmore, 2013).

The water area of all reaches both in flood season and non-flood season, increased significantly after 2000, with more increment in flood season. Compared with 1990s, the $\widetilde{R_W}$ in the flood season increased by about 0.016 ~ 0.192 in 2000s. Compared with 2000s, the $\widetilde{R_W}$ during flood season in 2010s increased by 0.018 and 0.021 in the Chumaer and Tuotuo River Reaches and decreased by 0.004 ~ 0.157 in other reaches. With little decrease in 2010s, the $\widetilde{R_W}$ of flood season in 2010s increased by 0.000 ~ 0.088 compared with that in 1990s. The variation of R_W in non-flood season is less than that in flood season. Compared with 1990s, the $\widetilde{R_W}$ of all reaches in non-flood season increased by about 0.003 ~ 0.073 during 2000s, which was only about 19 ~ 38% increment of the flood season in the corresponding period. Compared with 2000s, the $\widetilde{R_W}$ of non-flood season in the Beilu and Tuotuo River Reaches both increased by 0.017 during 2010s, which decreased by 0.077 ~ 0.005 in other reaches. The $\widetilde{R_W}$ of flood season in 2010s increased by -0.010 ~ 0.058 compared with that in 1990s. The water area increased obviously in the 2000s, despite of slightly decreasing in the 2010s, which could be the result of the generally increased runoff after 2000.

In addition to the interdecadal variation of runoff, the interdecadal variation of R_W is also influenced by the R_W-Q relationship. The decadal mean annual runoff in the SRYR increased by 7.5% in the 2010s compared with that in the 2000s (Fig. 6), but the water area generally decreased slightly, indicating that the water area may not be solely controlled by runoff. For instance, the R_W-Q relationship of the Tuotuo River Reach did not change significantly from 1990 ~ 1999, 2000 ~ 2009, and 2010 ~ 2018 (Fig. S5). Therefore, with the increase of Q, the $\widetilde{R_W}$ in the Tuotuo Reach increased in the 2010s compared to the 2000s. Lack of long-term daily discharge data makes it impossible to analyze the changes of R_W-Q relationship in other reaches. It is speculated that the decreasing in R_W of remaining reaches in the 2010s, may be the result of the change of the R_W-Q relationship.

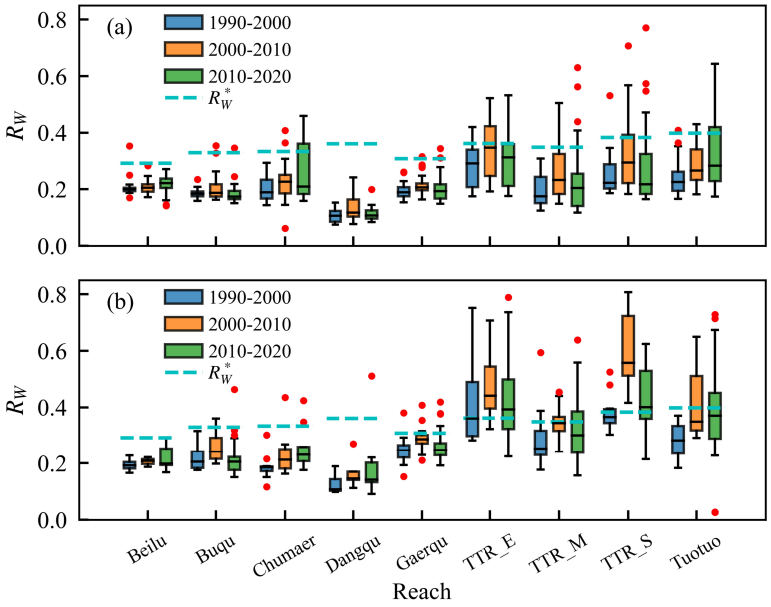

Figure 11. Inter-decadal variation of R_W in different braided reaches. (a) non-flood season (May ~ June, September ~ October), (b) flood season (July ~ August).

The braided reaches in the SRYR have different degrees of channel expansion. The channel expansion rates (M_R) in the Chumaer, Beilu, *TTR_M*, *TTR_S*, Gaerqu, Tuotuo, Buqu, Dangqu and *TTR_E* Reaches were 1.14, 1.88 1.49, 0.57, 0.57, 0.41, 0.27, 0.15, and 0.07 m/a, respectively. Riverbank vegetation conditions, soil types, and valley confinement determine the erosion resistance ability of riverbank. The water and sediment flux in the SRYR increased significantly after 2000 (Fig. 6), which would increase the active range of braided channels and strengthen the capability of bank erosion. Therefore, channels in the 9 reaches expanded to varying degrees. The soil type in the Chumaer and Beilu River Reaches is desert soil, banks are unconsolidated and widely distributed with gullies (Fig. S13), and the erosion resistance is weak. Therefore, M_R in these two reaches is relatively larger than that in other 7 reaches. Owing to the well-developed riparian vegetation, the erosion resistance is strong in the Dangqu and Buqu River Reaches, which led to the rather low M_R. The Gaerqu River Reach is closer to the source of glaciers, with sufficient sediment supply and poor riparian vegetation than that of Dangqu and Buqu River Reaches, so the M_R is slightly larger. Inundation chance of *TTR_S*, *TTR_M*, *TTR_E* and Tuotuo River Reaches is high, and the flow erosion capability is strong. Because *TTR_E* Reach is in a confined valley parallel to the river flow direction, the M_R is the smallest among all reaches. While the river flow direction of *TTR_M* Reach is orthogonal to the mountain range, large scale erosion occurs on the local unconfined bank (Fig. S8), and the M_R is large (second

only to the Beilu River Reach). *TTR_S* and Tuotuo Reaches are both unconfined channels, which are affected by the increases of water and sediment flux and have a large M_R. The increase of water and sediment flux makes the braided channel generally expand.

River channel expansion occurs mostly in the local banks with interfluve and abandoned branches because of weak confinement. The channel expansion mostly occurs in the local riverbank (Fig. S6 ~ S8 and S10 ~ S12), except for the global expansion of Chumaer and Beilu River Reaches due to unconsolidated riverbanks. Channel expansion mostly occurs on weakly restricted riverbanks with abandoned branches or interfluve (Fig. S6 ~ S12). The abandoned branch may be a historical trace left during lateral migration of the river channel, or it may be a new branch formed by the temporary cutting from the river bank during flood event (Ashmore, 2013). Given that the new branch continues to develop into a permanent branch, the interfluve between the new branch and the original river channel will come into being. The characteristic of abandoned branch is that its branch elevation is slightly higher than that of the active branch, but lower than that of the land outside riverbank. Therefore, when the water and sediment flux increase, the water flow will transport bedload sediment along the abandoned branch, forming a continuous branch and an interfluve, hence the channel expanded. Meanwhile, the interfluves shrunk by varying degrees (Fig. S6, S8, S9 and S12), which may be related to the enhancement of lateral migration intensity caused by the increase of water and sediment flux (Fig. 13). Thus, the presence of interfluve and abandoned branches indicates that banks here are more prone to be eroded when the water and sediment flux increase in braided rivers.

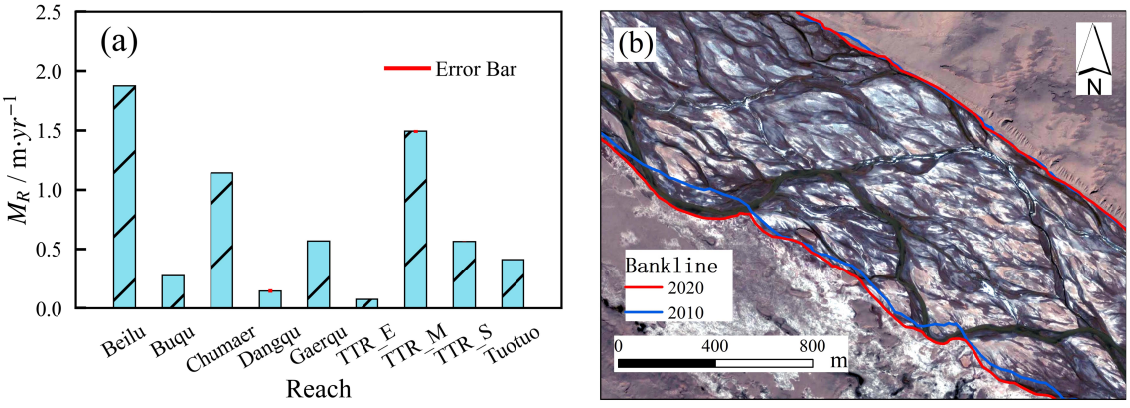

Figure 12. General channel expansion of braided rivers in the SRYR. (a) Channel expansion rates of each braided reach from 2000 ~ 2012 to 2020 (b) Bank expansion of the Beilu River Reach from 2010 to 2020.

The migration intensity in all reaches shows various trends of strengthening, unchanged, and weakening. The average migration intensity $\overline{IM_I}$ of 3 ~ 5 years was used to reflect the variation trend of migration intensity, based on the study of migration intensity at different temporal scales (Fig. 10). The migration intensity in the Tuotuo, Gaerqu, Chumaer, and Beilu River Reaches showed an increasing trend over time (r=0.57 ~ 0.90, p=0.04 ~ 0.19), among which the Gaerqu River Reach showed a significant increasing trend (r=0.9, p=0.04). The $\overline{IM_I}$ of these reaches increased by 0.016, 0.022, 0.051 and 0.038 from 1990 ~ 1995 to 2016 ~ 2020, respectively. The $\overline{IM_I}$ of *TTR_S*, *TTR_M* and *TTR_E* Reaches did not change significantly with time, and $\overline{IM_I}$ remained at the level of 0.078, 0.052 and 0.097, respectively, with p=0.62 ~ 0.76. The $\overline{IM_I}$ of the Buqu River Reach showed a significant decreasing trend (r=-0.69, p=0.06). The change trend of $\overline{IM_I}$ in the Dangqu River Reach was flat, with average value of $\overline{IM_I}$=0.010, which indicates a very weak migration capability (Fig. 13e, Fig. 10).

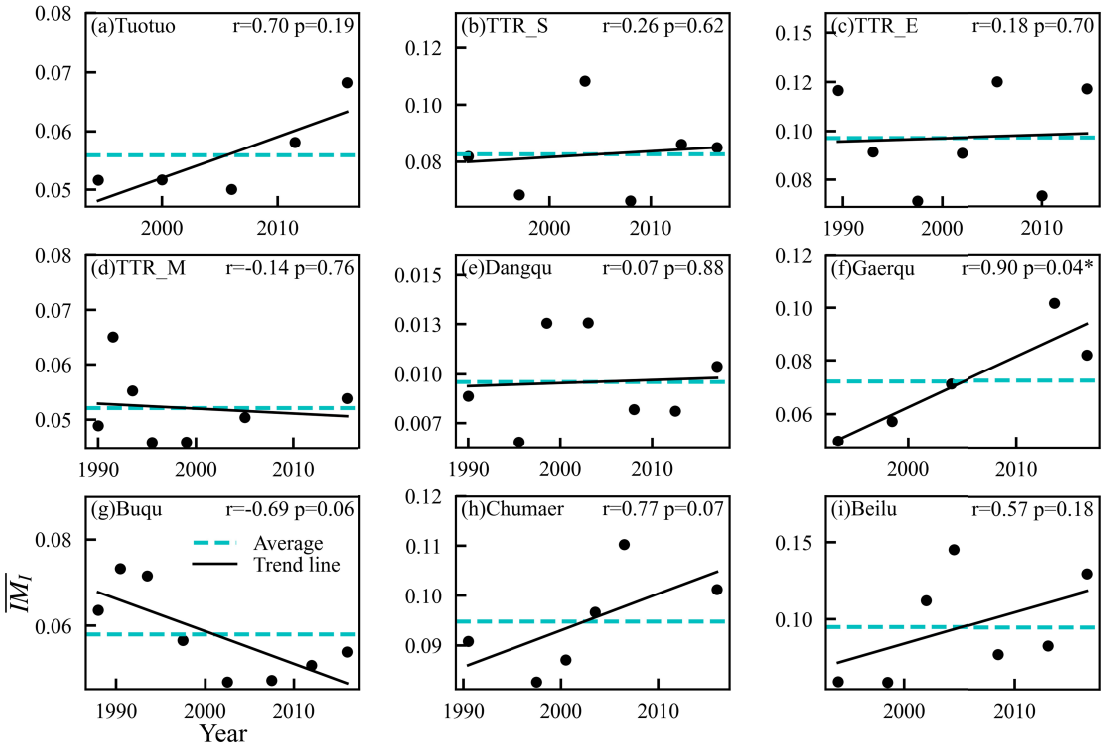

Figure 13. Migration intensity variation trends of 9 braided river reaches in the SRYR (mark * denotes the significance level of $p<0.05$).

3.5 Response of migration intensity to the hydrograph

The intra-annual migration intensity IM_I of the braided channel is related with the long inundation time, that is, IM_I mainly depends on whether the year is of high flow or low flow. There is a positive power law relationship between the migration intensity IM_I in the Tuotuo River Reach and the annual maximum discharge $Q_{\max}$ (Fig. 14a, Eq. (19)).

$$IM_I \propto Q_{\max}^{\beta} \tag{18}$$

where β is a power exponent and Q_{max} is the maximum annual discharge. Intra-annual migration intensity IM_I and maximum annual discharge Q_{max} in the Tuotuo River Reach conform to the function of $IM_I=0.0208Q_{\max}^{0.417}$, with $\beta=0.417$. It means that the higher annual maximum discharge, the greater migration intensity in the channel after water overflows the sandbars (Lu et al., 2022; Shampa and Ali, 2019; Sonke et al., 2022).

After 2009, the migration resistance in the Tuotuo River Reach was enhanced. The relationship between IM_I and annual runoff in the Tuotuo River Reach has changed significantly after 2009. As shown in Fig. 14a, the annual runoff and Q_{max} in the Tuotuo River in 1995 were 0.712×10^9 m^3 and 185 m^3/s, respectively, and were 0.688×10^9 m^3 and 171 m^3/s in 2015. The runoff, annual maximum discharge, and hydrograph in 2015 were similar to those in 1995 (see Fig. S14), but the IM_I in 2015 was 0.123, only 54% of that in 1995 (IM_I=0.226). The *NDVI* value of the Tuotuo River Reach in 1993 ~ 1995 was 0.081, which was lower than that of 2014 ~ 2016 (*NDVI* = 0.102) (Fig. S16b). This indicates that the growth of sandbar vegetation and riverbed resistance in channel after 2010 resulted in a smaller IM_I in dry year (2015). The $Q_{\max}$ and IM_I (397, 0.232) of 1996 were similar to those of 2014 (386, 0.242), although the annual runoff of the latter year was larger than the former year (i.e., longer inundation time). This is because, the

channel *NDVI* value of 2014 (0.102) was higher than that of 1996 (0.075), erosion resistance of riverbed was improved, led to similar IM_I between 1996 and 2014. The increase of riverbed resistance result in the decrease of migration intensity in dry years.

After 2000, the continuous effect of high discharge eliminates the influence of vegetation growth on migration intensity, and the migration intensity in the Tuotuo River Reach shows an increasing trend. The runoff in the Tuotuo River increased significantly in late 1990s, from Q_{max}= 97 ~ 294 m^3/s during 1985 ~ 1995 to Q_{max} = 166 ~ 600 m^3/s during 1996 ~ 2018, and Q_{max} increased by 1.71 to 3 times. The increase of Q_{max} enhances the migration intensity perennially, regardless of the enhanced bed erosion resistance caused by the growth of sandbar vegetation. Meanwhile, owing to the positive correlation between water and sediment flux in this reach (Li et al., 2020d), a large increase in runoff flux indicates a large increase in the suspended sediment flux. The dominant factors of IM_I are the increases of the water and sediment flux, which make $\overline{IM_I}$ of the Tuotuo River Reach display an increasing trend after 2000 (Fig. 13a).

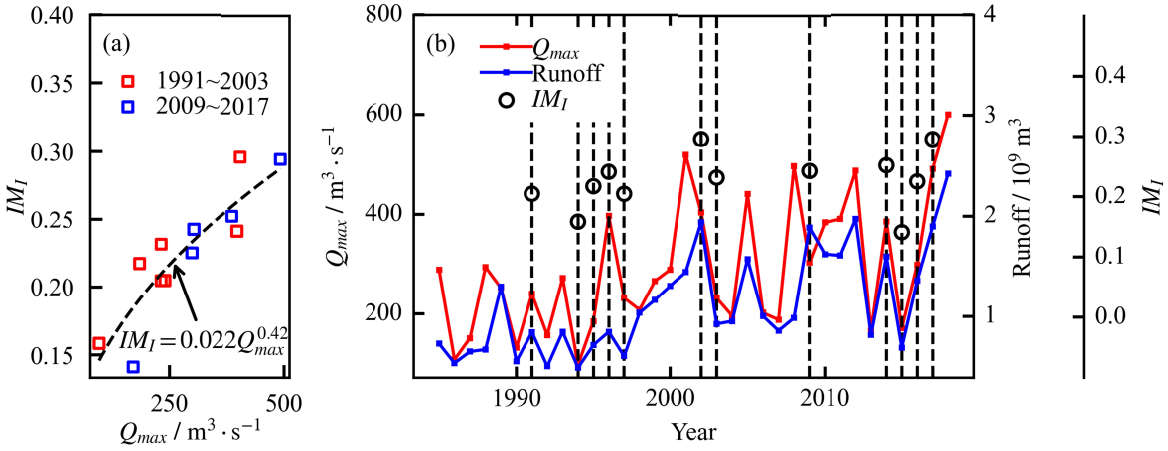

Figure 14. Influencing factors of migration intensity in the Tuotuo River Reach. (a) The correlation between annual migration intensity IM_I and annual maximum discharge Q_{max} in the Tuotuo River Reach (b) The inter-annual changes of annual maximum discharge and annual runoff in the Tuotuo River Reach.

The migration resistance of *TTR_M* Reach in the Tongtian River is also enhanced. The annual migration intensity IM_I of the *TTR_M* reach is positively power law correlated with the annual maximum discharge Q_{max}, with the power exponent of 0.417 (Fig. 15d). In 2007, Q_{max} is 2240 m^3/s, and the annual runoff was 13.555×10^9 m^3, IM_I=0.166. In 2013, Q_{max} is 2160 m^3/s, and the annual runoff was 13.290×10^9 m^3, which was similar to 2007, while IM_I=0.137, which was 17.5% smaller than 2007. This is owing to the growth of sandbar vegetation after 2010, with *NDVI*=0.104 during 2005 ~ 2007 and *NDVI*=0.126 during 2011 ~ 2013. After 2000, the water and sediment flux in the Tongtian River increased, and the annual maximum discharge and annual runoff increased significantly, which enhanced the migration intensity of the braided channel in high flow years. For example, Q_{max}=2860 m^3/s in 1991 is close to Q_{max}=2960 m^3/s in 2014, but the runoff in 2014 is 18.620×10^9 m^3, which was 48.4% higher than 12.550×10^9 m^3 in 1991. In this case, the *NDVI* is 0.131 during 2014 ~ 2016, obviously higher than that in 1990 ~ 1992 (*NDVI* = 0.112), which means the enhanced erosion resistance. Still, long term effect of high flow makes the migration intensity IM_I (0.209) in 2014 higher than that in 1991 (IM_I = 0.174). Similar to the Tuotuo River Reach, although the migration resistance of the *TTR_M* Reach is enhanced, the migration intensity is still controlled by the high flow condition.

With the same discharge increasing rate, the water area ratio in the *TTR_M* Reach increases more than that of the Tuotuo River Reach. According to the calculation formula of R_W (Eq. (2)), for the same reach, $R_W=A_W/A=L*W_e/A$, where W_e is the effective water surface width (Ashmore and Sauks, 2006), river length L and river area A are constant, so R_W is proportional to W_e. As a hydraulic geometric parameter of reach scale, W_e is more stable in braided rivers than the surface width of cross-section scale (Ashmore and Sauks, 2006; Peirce et al., 2018). R_W can be used as a proxy for W_e in reach scale, thereby establishing a power law relationship with flow (Eq. (20), Fig. 15a, b).

$$R_W \propto Q^b \tag{19}$$

where Q is the immediate discharge and b is the power exponent. In Fig. 15a, b, the R_W-Q relationship of the *TTR_M* and Tuotuo River Reaches is $R_W=0.0038Q^{0.625}$ and $R_W=0.0658Q^{0.384}$, respectively, and the exponent b is 0.625 and 0.384, respectively. The b index of *TTR_M* reach is about 1.63 times higher than that of the Tuotuo River Reach, indicating that the river channel of *TTR_M* Reach is wider and shallower than that of the Tuotuo River Reach (Ashmore and Sauks, 2006; Smith et al., 1996).

The inter-annual discharge increase of *TTR_M* Reach in the Tongtian River is relatively small, which it is not enough to enhance the migration intensity since the vegetation of the sandbar increases. During 1990 ~ 2000, Q_{max} is 1030 ~ 2890 m^3/s in the Tongtian River, and after 2000, Q_{max} is 1490 ~ 3700 m^3/s, with a relatively small increase range of 28% to 45% compared to that in the Tuotuo River (71% ~ 200%). As shown in Fig. 15a, b, based on the R_W-Q relationship, when R_W=0.6, Q is 3580 m^3/s in the Tongtian River, which only occurs in 2005. In the Tuotuo River, R_W=0.6 corresponds to Q=315 m^3/s. After 2000, there were 10 years of which the maximum annual discharge was greater than 315 m^3/s. Although the water and sediment flux in both the Tuotuo and Tongtian Rivers have increased significantly since 2000, the maximum flow increase in the Tongtian River is not as large as that in the Tuotuo River. Therefore, compared with the increase in riverbed resistance caused by vegetation growth, increase trend of the migration intensity in the Tongtian River is not obvious (Fig. 13b, c, d).

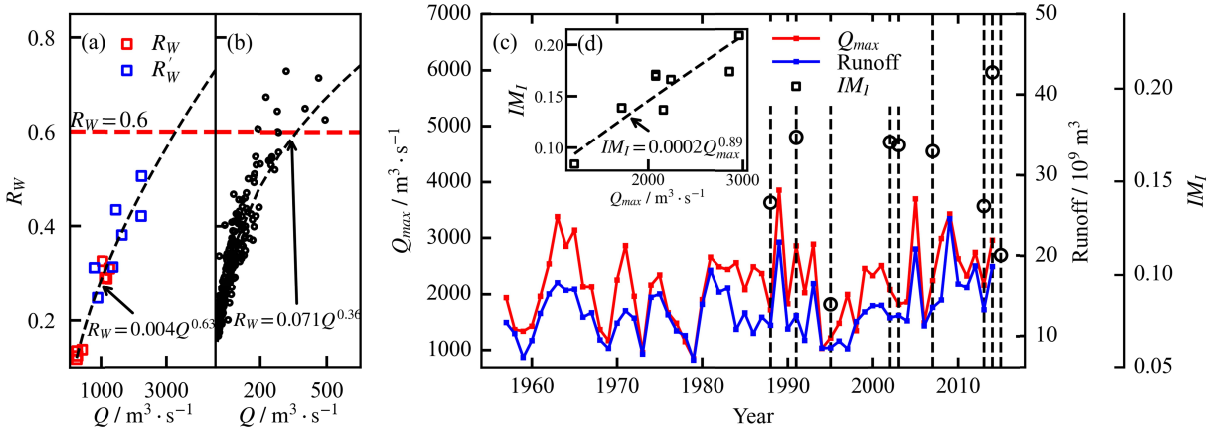

Figure 15. Influencing factors of migration intensity in the Tongtian River. (a and b) The R_W-Q Relationship of *TTR_M* (the Middle Reach of the Tongtian River) Reach and Tuotuo River Reach (R_W' is the water area ratio of image that was partially obscured by cloud, which estimated based on reference image in accordance with Section 2.2.7). (d) The correlation between the annual migration intensity IM_I and the annual maximum discharge Q_{max}, and (c) The inter-annual variation of the annual maximum discharge Q_{max} and the annual runoff of the Tongtian River.

4 Discussion

4.1 The advantage of the new method for extracting braided water body

The Local Otsu + Lowpath method is proposed in this study to improve the recognition accuracy of braided water complexity. When the branch width of braided river is smaller than the image resolution, the small branch will only pass through one pixel in the transverse direction (reducing the *MNDWI* value of the pixel on average). Although the *MNDWI* value of this pixel is still significantly higher than that of the land area and can also be identified by visual estimation (Fig. 2), its *MNDWI* peak value is significantly lower than that of the wider branch pixel (Fig. 2). Therefore, the single threshold method cannot properly extract all branches (Fig. 4), which lead to underestimated braiding intensity. Using the combined method of Local Otsu method (Farrahi Moghaddam and Cheriet, 2012, 2010; Nicolaou et al., 2014) and Lowpath method (Hiatt et al., 2020), the morphological complexity of braided rivers can be fully identified, which is close to the true value of visual interpretation (Fig. 4).

It should be noted that this method is not necessary in all cases of braided river segmentation. For braided rivers with wide branches, such as the Yarlung Tsangpo River on the southern QTP, in which the branch width is larger than 30 m (Han et al., 2023; Shampa and Ali, 2019; You et al., 2022), can simply use the Global Otsu method to extract water bodies. Small branches (<10 m) are commonly exist in braided rivers in the SRYR (Ma et al., 2021), which is suitable for the application of Local Otsu + Lowpath method. Owing to the limited resolution of remote sensing images, the complexity of braided rivers will be underestimated, and the Local Otsu + Lowpath method can identify the river information as fully as possible.

4.2 Consistent characterization of morphological parameters of braided river

There are well-functional relationships between dimensionless parameters of braided river morphology. The morphological characteristics of braided rivers change dramatically with the increase of water area (Li et al., 2018; Lu et al., 2022; Shampa and Ali, 2019). Braiding intensity B_{T3} has a good parabolic function relationship with water area ratio R_W (Fig. 7) (Li et al., 2020d), which conforms to the function $B_{T3}(R_W) = a(R_W - R_W^*)^2 + B_{T3peak}$. The peak of the parabola indicates the maximum braiding intensity B_{T3peak} that a braided river can reach, with corresponding water area ratio R_W^*. R_W^* is 0.29 ~ 0.40 in 9 braided rivers of the SRYR, and B_{T3peak} is significantly positively correlated with the average channel width (Fig. 7). The average sandbar area ratio $\overline{R_b}$ in a braided channel is negatively power law correlated with R_W (Fig. 8), which conforms to $\overline{R_b} \propto 1/R_W^{\alpha}$. The larger the exponent α, the higher the degree of fragmentation of the sandbars in the channel. The higher α may be the result of higher braiding intensity and higher the inundation chance, which means more intensively cutting of sandbars (Fig. 9). The parabolic relation of B_{T3}-R_W and the negative power law relation of $\overline{R_b}$-R_W generally exist in the braided rivers of the SRYR. The functional characteristic parameters α, R_W^*, B_{T3peak} of the fitting function B_{T3}-R_W and $\overline{R_b}$-R_W can be used to characterize the morphological characteristics of braided rivers in the reach-scale more comprehensively.

4.3 Impacts of warming and wetting climate on morphological changes of braided river

Located in the hinterland of the QTP, the SRYR is strongly responsive to climate warming. From 1957 to 2020, the river basin shows a consistent warming and wetting trend (Fig. 5). Air temperature and precipitation have increased significantly since 1990 and 2000 (Ahmed et al., 2023; Deng et al., 2022; Ji et al., 2021; Li et al., 2013a, 2013b, 2023b). It resulted in the increase of vegetation abundance and river channels after 2000 (Fig. S16) (Ji et al., 2021), and the water

and sediment flux in the river basin increased significantly after 2000 (Fig. 6) (Ahmed et al., 2022; Hu et al., 2022; Ji et al., 2021; Li et al., 2020a, 2023b; Sun et al., 2022).

Climate warming lead to the receding result of permafrost (Li et al., 2013b; Wang et al., 2017b; Yang et al., 2011) and the melting of glacier-snow in the SRYR (Gao et al., 2014, 2014; Li et al., 2021a; Liu et al., 2017; Wang et al., 2017a; Yang et al., 2003). The permafrost temperature of 0 ~ 20 cm soil in the SRYR increased by 0.2 ~ 0.3 ℃ from 1968 to 2008 (Li et al., 2013b), which cause permafrost to retreat. The glaciers in the SRYR are mainly distributed in the western section of the Tanggula Mountains, that is, the source of the Tuotuo, Buqu, Gaerqu and Dangqu Rivers. In recent 50 years, the glacier has retreated and thinned (Gao et al., 2014; Wang et al., 2017b; Wu et al., 2013), with 11.98% decrease in the glacier area and 25 completely disappeared glaciers from 1990 to 2015 (Wang et al., 2017a). From 1969 to 2009, the glacier area in the Tuotuo River Basin decreased by 20.83% (Gao et al., 2014; Wang et al., 2017b; Wu et al., 2013), and by 34.81% in the Buqu River Basin (Wu et al., 2013). Typical glaciers such as the Gangjiaquba Glacier (the source region of the Gaerqu River) and Jianggendigru Glacier (the source region of the Tuotuo River) retreated 4470 m and 3200 m, respectively, from 1977 to 2009 (Gao et al., 2014). Climate warming causes changes in the freeze-thaw cycle and prolongation of the thawing process in the SRYR (the initial freezing date of the year is delayed by 13.5 days /10a) (Li et al., 2023a). Climate change also changes the precipitation type in the river basin, the proportion of snow in the precipitation decreases by 2.50% /10a, which mainly occurs in the area above 4500 m a. s. l. The SRYR is the main permafrost on the QTP, and the glacier, permafrost, and snow in the source region strongly respond to climate warming.

The warming and wetting in the SRYR Basin led to the general growth of vegetation in the river basin and the sandbars after 2000. The *NDVI* value of the SRYR decreased from 1988 to 2000 (Li et al., 2021c) and had an abrupt increase in 1998 (Ji et al., 2021), *NDVI* of the river basin increased significantly after 2000 (Fig. S16c). In recent 30 years, *NDVI* value has shown an overall increasing trend (Wang et al., 2022) in the SRYR, 96.9% of the area showed an increasing trend of *NDVI* from 1990 to 2020 (Fig. S16b), and *NDVI* value increased most in the southeast part. The *NDVI* value of sub-basins increased 0.059 ~ 0.084 from 1990 to 2020. The *NDVI* value of river channels change little before 2005 and increased obviously after 2006, with 12.2 ~ 52.9% increment from 2006 to 2018. The spatial distribution of *NDVI* is consistent with the spatial distribution of hydrothermal conditions (Fig. S16a). This is because the combined effects of climate warming and permafrost change are the main causes of fluvial geomorphic changes in the alpine ecosystem in the SRYR (Li et al., 2013b). In the 2000s, *NDVI* values of the SRYR were positively correlated with shallow ground temperature, air temperature and precipitation, and the correlation between *NDVI* value and shallow ground temperature increased with depth (Yang et al., 2011; Zhao et al., 2020). Therefore, the thawing of permafrost, the shortening of the freezing time of active layer (Li et al., 2023a), and the increase of shallow ground temperature (Li et al., 2013b) are conducive to the growth of vegetation and the increase of *NDVI*. In the past 30 years, the improvement of hydrothermal condition is the main reason for the growth of vegetation in the river basin and river channels in the SRYR (Liu et al., 2014).

The warming and wetting in the SRYR also resulted in the increase of runoff after 2000. In the past 30 years, the annual runoff in the SRYR at the ZMD Station showed a continuous decrease trend before 2005, and a significant increase trend after 2005 (Ji et al., 2021). The annual runoff increased by 36.36% and 7.49% in 2000s and 2010s, respectively (Fig. 5). Runoff in the SRYR is supplied by precipitation (34%), permafrost (49%), and meltwater from glaciers and snow (17%) (Li et al., 2020c). Precipitation, as the main supply term of surface water

resources, has the most significant contribution to runoff. Taking the Tuotuo River Basin as an example, the effects of meteorological factors on runoff is precipitation > air temperature > evaporation (Luo et al., 2020). Annual precipitation increased by 44.3 mm in the 2000s and -8.7 mm in the 2010s (Fig. 5), this is the direct cause of runoff increase in the SRYR after 2000 (Ahmed et al., 2023; Wu et al., 2013). At the same time, the rising temperature causes the melting of glaciers and snow cover, and the change of permafrost active layer also promotes the recharge of discharge (Qi et al., 2015; Wang et al., 2009; Zhang et al., 2008). For instance, the runoff from the glacier retreat during 1969 ~ 2009 accounted for about 3.77% of the total runoff of the Tuotuo River during this period (Wang et al., 2017b). The mean annual runoff in the Buqu River is 27.42 m^3/s (Wu et al., 2013), and the glacier recharging runoff accounts for 3.68%. Runoff in the SRYR is more responsive to climate change than land cover change (Ahmed et al., 2022; Wang et al., 2017b). Thus, the rising of air temperature and precipitation makes the runoff of the SRYR increase significantly after 2000.

Climate warming is the main reason for the increase of sediment flux in the SRYR. Sediment flux comes from hillslope (surface flow erosion), channel erosion, and glacier erosion. The thawing permafrost caused by climate warming (Li et al., 2013b) results in the significant increase of erodible area from 1985 to 2017 in the SRYR (Li et al., 2021b). At the same time, the extension of the melting process (Li et al., 2023a) will prolongs the time that the surface can be eroded. Owing to increased runoff and surface temperature, more sediment load is transported into rivers through surface soil erosion, resulting in increased sediment flux (Li et al., 2023a).

In summary, with the increase of precipitation after 2000 and continued increase of air temperature after 1990, the glacier, snow and permafrost melted, and the vegetation coverage increased after 2000 (Ji et al., 2021; Wang et al., 2022; Yang et al., 2011), and the water and sediment flux also increased after 2000 (Li et al., 2020a, 2023a). The increase of water and sediment flux in the braided river system is manifested as the increase of water area, the erosion of riverbank, and the change of the migration intensity of branches. (i) After 2000, the significantly increased runoff led to a substantial increase in the water area of each braided reach in the 2000s and 2010s, compared with that in 1990s (Fig. 11). (ii) The increase of the water and sediment flux also strengthened the erosion capability of water flow to the riverbank, which led to the universally expansion of braided channels in the past 20 years (Fig. 12). Moreover, river channel expansion mostly occurs in local riverbanks with abandoned branches or interfluves (Fig. S6 ~ S12). (iii) It is worth noting that the increase of the water and sediment flux will lead to the intensification of riverbed evolution (Li et al., 2018; Limaye, 2020; Peirce et al., 2018; Shampa and Ali, 2019; Smith et al., 1996), which will enhance the migration intensity in the channel. However, under the same impact of climate warming and wetting, vegetation abundance in the river basin and river sandbar also increased after 2000. The increase of vegetation abundance would slightly enhance the erosion resistance of riverbed, limits the increase of sediment supply and sediment transport capacity of the river basin, hence restricts the increase of migration intensity. Therefore, the intra-channel migration intensity in the braided reaches presents three different trends (Fig. 13).

4.4 Three patterns of migration intensity in response to water and sediment flux change

In the past 30 years, the temporal variation trend of the migration intensity in 9 braided reaches of the SRYR region can be summarized into three categories: (1) Beilu, Chumaer, Tuotuo, and Gaerqu River Reaches showed an increasing trend; (2) Dangqu, *TTR_S*, *TTR_M* and *TTR_E* Reaches showed no obvious trend; (3) Buqu River Reach showed a decreasing trend

(Fig. 13). The causes of the variation trend of the migration intensity of each braided reaches from 1990 to 2020 are analyzed below.

The variation of the migration intensity is affected by the annual runoff, sediment recharge and the change of riverbed erosion resistance (the braided river in the SRYR is not almost affected by human activities). It should be noted that glacier retreat contributed about 6.8% to runoff of the Tuotuo River (Wang et al., 2015) and 15.0% to runoff in the Gaerqu River (Liu et al., 2016). It should be considered that the impact of glacier retreat (mainly the glaciers in the Tanggula Mountains) on migration intensity is mainly limited in braided reaches near glaciers. The effect of glacier change is not considered here (all study reaches are close to the outlet of the river basin). There is a lack of water and sediment data (only TTH and ZMD Station), in the flood season (which is the main period of braided river evolution) median value of water area ratio ($\widetilde{R_W}$) to reflect the runoff level of the reach. Using the mean annual *NDVI* of the catchment area ($\overline{\mathrm{NDVI}_{Catch.}}$) to reflect the overall erosion resistance level of the catchment area, which of the river channel ($\overline{\mathrm{NDVI}_{Chan.}}$) was used to reflect the erosion resistance of the riverbed (Fig. 16). The migration intensity IM_I* calculated by 30-year interval images from 1990 to 2020 reflects the migration intensity of each braided reach.

According to the aforementioned indices, the response of braided reaches to climate warming can be divided into three patterns: (a) Sediment Increase Constrained Pattern (SICP), (b) Sediment Increase Dominated Pattern (SIDP), and (c) Runoff Increase Dominated Pattern (RIDP). The response mechanism of different patterns in large braided rivers to climate warming is shown in Fig. 17.

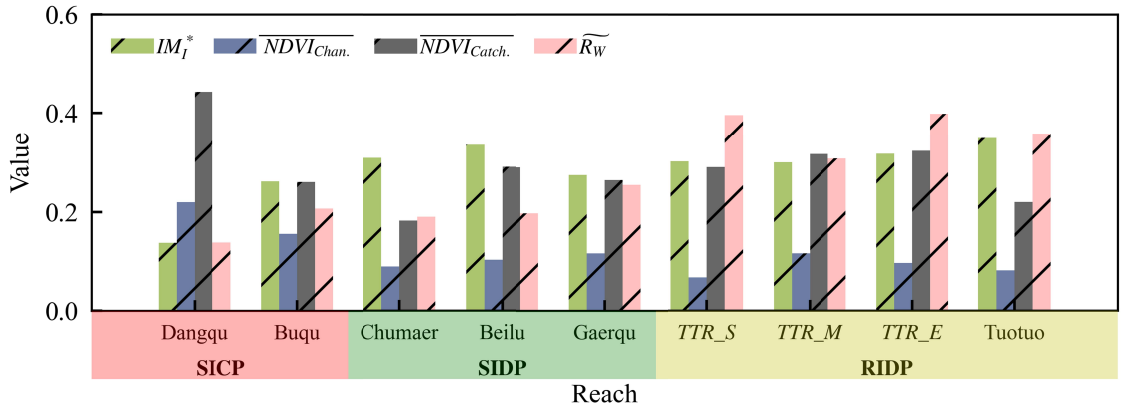

Figure 16. The migration intensity IM_I* in each braided reach from 1990 to 2020, mean annual *NDVI* value for channel $\overline{NDVI_{Chan.}}$, mean annual *NDVI* value of catchment area $\overline{NDVI_{Catch.}}$, median water area ratio $\widetilde{R_W}$ in flood season from 1990 to 2020.

(1) Sediment Increase Constrained Pattern: This type of braided river has a low probability of inundation and limited sediment recharge due to the influence of upstream topography or vegetation growth in the catchment area. Meanwhile, the vegetation abundance of the sandbar is high, and the erosion resistance capability of the riverbed is strong (Fig. 16). The migration intensity in the channel of such rivers is weakly affected by the increase of the water and sediment flux, hence the migration intensity trend remains unchanged (Dangqu River Reach) or decreases (Buqu River Reach) (Fig. 17).

Wetland filtration in the upper reaches of the Dangqu River makes the river pattern of the Dangqu River Reach stable, so there is no obvious variation trend of migration intensity. The Dangqu River Reach is located at the upstream of the Dangqu River, and its catchment area is a damp, low-lying area, which is full of marsh wetlands (53.52% of the Dangqu River wetlands

mainly distributed in the 4700 ~ 5000 m area (Zhao et al., 2020)). The Dangqu River Reach has the lowest inundation chance ($\widetilde{R_W}$=0.138), and the highest vegetation coverage in its catchment area ($\overline{NDVI_{Catch.}}$=0.443) which limits sediment yield (Fig. S16a). While the highest vegetation abundance on the sandbar ($\overline{NDVI_{Chan.}}$=0.220) results in strong migration resistance and stability of the riverbed (Fig. 16). As a result of the above factors, the river pattern of the Dangqu River Reach is stable and the level of migration intensity is extremely low (IM_I*=0.138), the sandbars are stable and almost become anabranching river type (Fig. S15, Fig. 10). High vegetation coverage in the upstream catchment will limit the increase of sediment flux, and the growth of vegetation on the sandbar will further strengthen the erosion resistance of sandbars. Therefore, the increase of water and sediment flux has little effect on the change of the channel migration intensity (Fig. 13e).

The inundation chance of the Buqu River Reach is low ($\widetilde{R_W}$=0.207), and the vegetation coverage of the catchment area and sandbar is low ($\overline{NDVI_{Catch.}}$=0.261 and $\overline{NDVI_{Chan.}}$=0.156) (Fig. 16). Glaciers develop in the upper reaches of the Buqu River, the terrain is relatively gentle, and the sediment in the source area is partly deposited in the Wenquan River Basin above a node in the upstream, which limited the sediment flux increase. The low inundation chance of the Buqu River Reach allows the vegetation on sandbar to grow, the erosion resistance of the riverbed is enhanced. Limited sediment increase result in the decreasing of migration intensity of the Buqu River Reach.

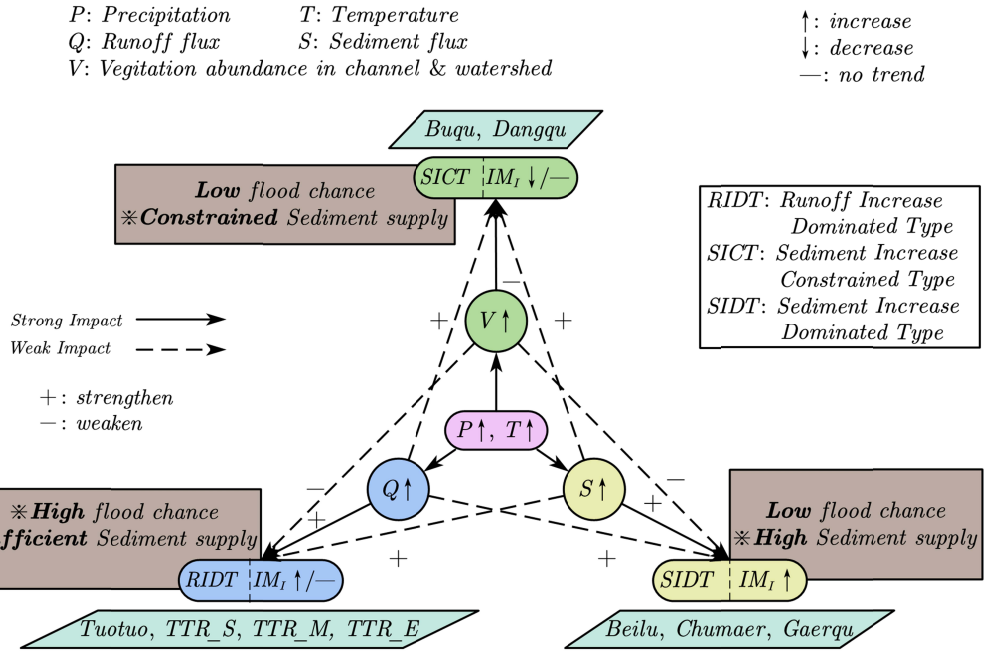

Figure 17. Different response patterns of migration intensity to climate warming in the SRYR.

(2) Sediment Increase Dominated Pattern: The vegetation in the catchment area of braided river is sparse and easy to be eroded, and the catchment topography is conducive to sediment yield. Although the inundation chance is low, the sediment recharge is excessive. The increase of sediment flux has a strong response to the increase of precipitation and air temperature. The excess sediment supply aggravates the migration of the branch in the river channel, with the weak erosion resistance, the migration intensity shows an increasing trend. The representative reaches of this type are Beilu, Chumaer, and Gaerqu River Reaches (Fig. 17).

The land cover in the Beilu and Chumaer River Basins is mainly bare land, and the sediment flux increase is strongly responsive to climate warming. The inundation chance of the Beilu and Chumaer River Reaches was not high ($\widetilde{R_W}$=0.197, 0.190). The level of *NDVI* in the catchment area of the Beilu River Reach was high (0.291), and the level of *NDVI* in the channel was low (0.103). The *NDVI* level in the Chumaer River Reach channel and the catchment area were both low (0.089 and 0.182). The migration intensity levels in the Beilu and Chumaer River Reaches (IM_I*=0.336, 0.309) were high (Fig. 16). The migration intensity of the Beilu and Chumaer River Reaches showed an obvious increasing trend. This is because the land type in the Beilu and Chumaer River Basins is desert soil (mainly bare land). As air temperature rises and permafrost thaws, more sediment material in this area will be transported into rivers. Therefore, when the precipitation increases, the sediment flux increases more and the sediment recharge is sufficient, and the migration intensity showed an increasing trend.

The land cover and catchment area vegetation abundance of the Gaerqu River Reach are similar to those of the Buqu River Reach, but the variation trend of migration intensity is the opposite to that of the Buqu River Reach (Fig. 16). The vegetation levels of the catchment area of the Buqu and Gaerqu River Reaches are identical ($\overline{NDVI_{Catch.}}$=0.261, 0.265). The proportions of bare land, grassland, and glacier area in Gaerqu River Basin are 40.94%, 51.83%, 5.53%, which are 46.67%, 48.85%, 3.13% in the Buqu River Basin (Yan et al., 2020). In general, the land cover types of the Gaerqu and Buqu River Basin are similar, but the migration intensity of the Gaerqu River Reach increases while that of the Buqu River Reach decreases (Fig. 13).

With higher inundation chance and sediment flux, and lower sand bar vegetation abundance, the Gaerqu River Reach showing an increasing trend of migration intensity. Compared with the Buqu River, the water and sediment flux of the Gaerqu River (Yan et al., 2020) and the migration intensity are both larger (Fig. 16). The Gaerqu River Reach has a substantially higher inundation chance than the Buqu River Reach ($\widetilde{R_W}$=0.255, 0.207), and the vegetation abundance of Gaerqu River Reach channel ($\overline{NDVI_{Chan.}}$=0.116) was substantially lower than that of the Buqu River channel ($\overline{NDVI_{Chan.}}$=0.156) (Fig. 16). When water and sediment flux increase, Gaerqu River channel will be less resistant to the erosion of flow, thus result in the increase of IM_I* (Fig. 16). Meanwhile, the Wenquan River Basin in the upper basin of the Buqu River can limit the increase of sediment flux, while the catchment area of Gaerqu River Reach is steeper, which is conducive to sediment yield in the river basin (Fig. S17). For above reasons, the migration intensity variation trend of the Gaerqu River Reach is dominated by increasing sediment flux and showing opposite trend with the Buqu River Reach.

(3) Runoff Increase Dominated Pattern: This type of braided river has a large annual inundation probability and a large increase in the water area during flood season. Owing to the high inundation chance, the impact of sandbar vegetation growth on the migration intensity is limited, and the migration of branches in the river is mainly affected by the discharge level. The annual migration intensity of the *TTR_M* and Tuotuo River Reaches has a positive power law correlation with the annual maximum discharge (Fig. 14a, 16d), and the runoff increase caused by climate warming is the key factor affecting the migration intensity of these rivers. The representative reaches are *TTR_S*, *TTR_M*, *TTR_E*, and Tuotuo River Reaches (Fig. 17).

The amplitude of runoff increase determines the variation trend of migration intensity. The inundation chance of *TTR_S*, *TTR_M*, *TTR_E* and Tuotuo River Reaches was higher ($\widetilde{R_W}$=0.396, 0.308, 0.399, 0.358). Frequent inundation resulted in low vegetation coverage on the sandbar in the channel ($\overline{NDVI_{Chan.}}$=0.067, 0.116, 0.096, 0.081) (Fig. 16). From the above analysis, the riverbed resistance in the Tuotuo and Tongtian Rivers are affected by the growth of sandbar

vegetation, especially in dry years. Compared with 1990-2000, the discharge in the Tuotuo River increased significantly after 2000, with the mean annual maximum discharge increasing by 60% and the mean annual runoff increasing by 86% (Fig. 14). The coefficient of variation (C_V) of the maximum annual discharge during 1990 ~ 2000 and after 2000 were both 0.396. Compared with the period from 1990 to 2000, the mean annual maximum discharge of the Tongtian River increased by 30% and the annual runoff increased by 42% after 2000, and the variation coefficient C_V of the annual maximum discharge decreased from 0.35 to 0.24. Therefore, the migration intensity of the three Tongtian River Reaches (*TTR_S*, *TTR_M*, *TTR_E*) showed no obvious change trend, while the migration intensity of the Tuotuo River Reach showed an increasing trend after 2000 (Fig. 13).

5 Conclusions

This study extracted water bodies from 9 braided river reaches in the Source Region of the Yangtze River on the Qinghai-Tibet Plateau during 1990 ~ 2020, based on the Google Earth Engine platform and using Landsat 5/7/8 and Sentinel-2 series remote sensing images. The empirical relationships of their morphology parameters were obtained and analyzed. Furthermore, combined with the meteorological and hydrological data, the impact of the water and sediment flux change driven by climate warming on the morphological characteristics of the braided river were quantitatively analyzed.

(1) Combining the Lowpath algorithm and the Local Otsu algorithm, a new water extraction method based on remote sensing images is proposed, which improves the accuracy of water complexity recognition, i.e., reducing 59% of the root mean squared error of braiding intensity in comparison with the Global Otsu method. This method is suitable for large braided rivers in which the branch width is smaller than the spatial resolution of the image.

(2) Because the channel morphology of braided river changes rapidly with the increase of water area, the braiding intensity B_{T3} and the water area ratio R_W of braided reach show a parabolic trend, and the average sandbar area ratio $\overline{R_b}$ and R_W show a negative power law trend. The characteristic parameters of the fitting function, such as the parabolic peak B_{T3peak} of B_{T3}-R_W, are positively correlated with the mean channel width, and the power exponent of $\overline{R_b}$-R_W function is negatively correlated with braiding intensity and inundation chance. In the parallel comparison of braided reaches, functional parameters can more comprehensively characterize the morphological characteristics of braided river.

(3) There is an obvious temporal scale effect on the intra-annual channel migration intensity of braided rivers. When the time span is less than 5 years, the migration intensity increases rapidly. However, when the time span is higher than 5 years, the migration intensity increases slowly. Thus, it is essential to consider the temporal scale effect when analyzing the change of the intra-annual channel migration intensity of braided river over time.

(4) The warming and wetting in the Source Region of the Yangtze River caused the increase of water and sediment fluxes, vegetation abundance of the river basin and sandbar, and led to the activation of braided rivers. With the increase of runoff, the active water area of each reach increased in both flood season and non-flood season after 2000, especially in flood season, indicating that the inundation chance of the braided rivers increased. With the increases of water and sediment flux, the channel of each river expands generally after 2000, and the bank erosion occurs mostly in the weak restricted bank with abandoned branch and interfluve. After 2000, the increase of vegetation on the sandbar enhanced the erosion resistance of the riverbed.

(5) The intra-annual channel migration intensity of braided rivers shows three trends of increasing, weakening and unchanged over time, and their response to climate warming can be divided into three patterns. (i) Sediment Increase Constrained Pattern (Buqu and Dangqu Rivers): rivers with high vegetation coverage or low topography in its catchment area and low inundation chance. The sediment flux increase caused by climate warming is limited, the vegetation on the sandbar has sufficient time to growth, and the erosion resistance of the riverbed is enhanced, so the migration intensity of the braided channel is weakened or maintained at a rather low level. (ii) Sediment Increase Dominated Pattern (Beilu, Chumaer, Gaerqu Rivers): the catchment area of braided river is characterized by loose soil and low vegetation coverage. Although the inundation chance of the river is low, the sediment flux increase of this type of river is strongly responsive to climate warming due to the high sediment transport rate, and the migration intensity of the braided channel shows an increasing trend. (iii) Runoff Increase Dominated Pattern (Tuotuo and Tongtian Rivers): for braided river with high inundation chance and high water and sediment fluxes, the variation trend of migration intensity is mainly affected by the increased amplitudes of water and sediment flux, showing an increasing or unchanged trend.

Acknowledgments

This study was supported by the National Natural Science Foundation of China (52239007, 51979012) and Central Public-interest Scientific Institution Basal Research Fund (Grant No. CKSF2021743 + CKSF2023311). We appreciate that Prof. Peng Gao gave valuable comments for the original manuscript.

Data Availability Statement

Remotely sensed data (Landsat 5/7/8 images courtesy of the U.S. Geological Survey) over the study area are available in the Earth Explorer repository at https://earthexplorer.usgs.gov/, and Sentinal imagery from the Google Earth Engine (GEE) platform. The meteorological data used in this paper are from the daily values of China surface data (SURF_CLI_CHN_MUL_DAY V3.0) and ERA5 data sets. data of annual water and sediment discharge at the Tuotuohe (1958-2018) and Zhimengda (1987-2014) Hydrological Stations were obtained from Qinghai Hydrological Bureau and Bulletin of China River Sediment (2000-2020). Data on morphological characteristics and temporal changes of the braided rivers are available online in Supporting Information.

References

Ahmed, N., Wang, G., Lü, H., Booij, M.J., Marhaento, H., Prodhan, F.A., Ali, S., Ali Imran, M., 2022. Attribution of Changes in Streamflow to Climate Change and Land Cover Change in Yangtze River Source Region, China. Water 14, 259. https://doi.org/10.3390/w14020259

Ahmed, N., Zhu, L., Wang, G., Adeyeri, O.E., Shah, S., Ali, S., Marhaento, H., Munir, S., 2023. Occurrence and Distribution of Long-Term Variability in Precipitation Classes in the Source Region of the Yangtze River. Sustainability 15, 5834. https://doi.org/10.3390/su15075834

Allen, S.K., Zhang, G., Wang, W., Yao, T., Bolch, T., 2019. Potentially dangerous glacial lakes across the Tibetan Plateau revealed using a large-scale automated assessment approach. Science Bulletin 64, 435–445. https://doi.org/10.1016/j.scib.2019.03.011

Ashmore, P., 2013. 9.17 Morphology and Dynamics of Braided Rivers, in: Treatise on Geomorphology. Elsevier, pp. 289–312. https://doi.org/10.1016/B978-0-12-374739-6.00242-6

Ashmore, P., Sauks, E., 2006. Prediction of discharge from water surface width in a braided river with implications for at-a-station hydraulic geometry. Water Resources Research 42. https://doi.org/10.1029/2005WR003993

Carlson, T.N., Ripley, D.A., 1997. On the relation between NDVI, fractional vegetation cover, and leaf area index. Remote Sensing of Environment 62, 241–252. https://doi.org/10.1016/S0034-4257(97)00104-1

Dee, D.P., Uppala, S.M., Simmons, A.J., Berrisford, P., Poli, P., Kobayashi, S., Andrae, U., Balmaseda, M.A., Balsamo, G., Bauer, P., Bechtold, P., Beljaars, A.C.M., van de Berg, L., Bidlot, J., Bormann, N., Delsol, C., Dragani, R., Fuentes, M., Geer, A.J., Haimberger, L., Healy, S.B., Hersbach, H., Hólm, E.V., Isaksen, L., Kållberg, P., Köhler, M., Matricardi, M., McNally, A.P., Monge-Sanz, B.M., Morcrette, J.-J., Park, B.-K., Peubey, C., de Rosnay, P., Tavolato, C., Thépaut, J.-N., Vitart, F., 2011. The ERA-Interim reanalysis: configuration and performance of the data assimilation system. Quarterly Journal of the Royal Meteorological Society 137, 553–597. https://doi.org/10.1002/qj.828

Deng, B., Xiong, K., Zhiyong, H., Jiang, C., Liu, J., Luo, W., Xiang, Y., 2022. Monitoring and Predicting Channel Morphology of the Tongtian River, Headwater of the Yangtze River Using Landsat Images and Lightweight Neural Network. Remote Sensing 14, 3107. https://doi.org/10.3390/rs14133107

Egozi, R., Ashmore, P., 2008. Defining and measuring braiding intensity. Earth Surf. Process. Landforms 33, 2121–2138. https://doi.org/10.1002/esp.1658

Farrahi Moghaddam, R., Cheriet, M., 2012. AdOtsu: An adaptive and parameterless generalization of Otsu's method for document image binarization. Pattern Recognition 45, 2419–2431. https://doi.org/10.1016/j.patcog.2011.12.013

Farrahi Moghaddam, R., Cheriet, M., 2010. A multi-scale framework for adaptive binarization of degraded document images. Pattern Recognition 43, 2186–2198. https://doi.org/10.1016/j.patcog.2009.12.024

Gao, P., Li, Z., You, Y., Zhou, Y., Piégay, H., 2022. Assessing functional characteristics of a braided river in the Qinghai-Tibet Plateau, China. Geomorphology 403, 108180. https://doi.org/10.1016/j.geomorph.2022.108180

Gao, S., Fan, Q., Cai, X., Ma, L., 2014. Glacial Fluctuation in the Source Region of the Yangtze River, in: H., G. (Ed.), 35th International Symposium on Remote Sensing of Environment (Isrse35). Iop Publishing Ltd, Bristol, p. 012135. https://doi.org/10.1088/1755-1315/17/1/012135

Gorelick, N., Hancher, M., Dixon, M., Ilyushchenko, S., Thau, D., Moore, R., 2017. Google Earth Engine: Planetary-scale geospatial analysis for everyone. Remote Sensing of Environment 202, 18–27. https://doi.org/10.1016/j.rse.2017.06.031

Guo, X., Gao, P., Li, Z., 2023. Morphodynamic Characteristics of a Complex Anabranching System in the Qinghai-Tibet Plateau and the Implications for Anabranching Stability. Journal of Geophysical Research: Earth Surface, 128, e2022JF006788. https://doi.org/10.1029/2022JF006788

Han, K., Sun, J., Lin, B., Huang, Z. Shi, X., 2023. Large-scale modelling of highly braided and laterally confined reach of sand-bed river. Earth Surface Processes and Landforms, 48, 1557-1572.

Hiatt, M., Sonke, W., Addink, E.A., Dijk, W.M., Kreveld, M., Ophelders, T., Verbeek, K., Vlaming, J., Speckmann, B., Kleinhans, M.G., 2020. Geometry and Topology of Estuary and Braided River Channel Networks Automatically Extracted From Topographic Data. J. Geophys. Res. Earth Surf. 125. https://doi.org/10.1029/2019JF005206

Hu, Y., Zhou, Y., Wang, Y., Lu, F., Xiao, W., Hou, B., Yu, Y., Liu, J., Xue, W., 2022. Impacts of Precipitation

Type Variations on Runoff Changes in the Source Regions of the Yangtze and Yellow River Basins in the Past 40 Years. Water 14, 4115. https://doi.org/10.3390/w14244115

Huang, W., Duan, W., Nover, D., Sahu, N., Yaning, C., 2021. An integrated assessment of surface water dynamics in the Irtysh River Basin during 1990–2019 and exploratory factor analyses. Journal of Hydrology 593, 125905. https://doi.org/10.1016/j.jhydrol.2020.125905

Ji, G., Song, H., Wei, H., Wu, L., 2021. Attribution Analysis of Climate and Anthropic Factors on Runoff and Vegetation Changes in the Source Area of the Yangtze River from 1982 to 2016. Land 10, 612. https://doi.org/10.3390/land10060612

Kendall, S.B., 1975. ENHANCEMENT OF CONDITIONED REINFORCEMENT BY UNCERTAINTY [1]. Journal of the Experimental Analysis of Behavior 24, 311–314. https://doi.org/10.1901/jeab.1975.24-311

Li, C., Jing, Z., He, X., 2021a. Remote sensing monitoring of glacier variation in Geladandong, source regions of the Yangtze River from 1986 to 2015. Journal of Glaciology and Geocryology 43, 405–416.

Li, D., Li, Z., Zhou, Y., Lu, X., 2020a. Substantial Increases in the Water and Sediment Fluxes in the Headwater Region of the Tibetan Plateau in Response to Global Warming. Geophys. Res. Lett. 47. https://doi.org/10.1029/2020GL087745

Li, D., Overeem, I., Kettner, A.J., Zhou, Y., Lu, X., 2021b. Air Temperature Regulates Erodible Landscape, Water, and Sediment Fluxes in the Permafrost-Dominated Catchment on the Tibetan Plateau. Water Resources Research 57, e2020WR028193. https://doi.org/10.1029/2020WR028193

Li, D., Wu, B., Chen, B., Qin, C., Wang, Y., Zhang, Y., Xue, Y., 2020b. Open-Surface River Extraction Based on Sentinel-2 MSI Imagery and DEM Data: Case Study of the Upper Yellow River. Remote Sensing 12, 2737. https://doi.org/10.3390/rs12172737

Li, J., Wang, G., Li, K., Li, Y., Guo, L., Song, C., 2023a. Impacts of climate change and freeze–thaw cycles on water and sediment fluxes in the headwater region of the Yangtze River, Qinghai–Tibet Plateau. CATENA 227, 107112. https://doi.org/10.1016/j.catena.2023.107112

Li, J., Wang, S., Qin, N., Liu, X., Jin, L., 2021c. Vegetation Index Reconstruction and Linkage with Drought for the Source Region of the Yangtze River Based on Tree-ring Data. Chin. Geogr. Sci. 31, 684–695. https://doi.org/10.1007/s11769-021-1217-5

Li, L., Shen, H., Dai, S., Li, H., Xiao, J., 2013a. Response of water resources to climate change and its future trend in the source region of the Yangtze River. J. Geogr. Sci. 23, 208–218. https://doi.org/10.1007/s11442-013-1004-z

Li, N., Wang, G., Liu, G., Lin, Y., Sun, X., 2013b. The ecological implications of land use change in the Source Regions of the Yangtze and Yellow Rivers, China. Reg Environ Change 13, 1099–1108. https://doi.org/10.1007/s10113-013-0419-5

Li, Y., Wang, H., Ma, Q., 2018. Responses of the braided channel to reduced discharge and lateral inputs of aeolian sand in the Ulan Buh Desert Reach of the Upper Yellow River. Environ Earth Sci 77, 379. https://doi.org/10.1007/s12665-018-7569-1

Li, Z., Li, Z., Feng, Q., Zhang, B., Gui, J., Xue, J., Gao, W., 2020c. Runoff dominated by supra-permafrost water in the source region of the Yangtze river using environmental isotopes. J. Hydrol. 582, 124506. https://doi.org/10.1016/j.jhydrol.2019.124506

Li, Z., Liu, M., Li, Z., Feng, Q., Song, L.-L., Xu, B., Liu, X., Gui, J., 2023b. Where does the runoff come from in dry season in the source region of the Yangtze River? Agricultural and Forest Meteorology 330, 109314. https://doi.org/10.1016/j.agrformet.2023.109314

Li, Z., Lu, H., Gao, P., You, Y., Hu, X., 2020d. Characterizing braided rivers in two nested watersheds in the

Source Region of the Yangtze River on the Qinghai-Tibet Plateau. Geomorphology 351, 106945. https://doi.org/10.1016/j.geomorph.2019.106945

Li, Z., Wu, Y., Hu, X., Yan, X., 2020e. Morphological similarity analysis of braided channel cluster in the Yangtze River source. Journal of Sediment Research 45, 13–20. https://doi.org/10.16239/j.cnki.0468-155x.2020.04.003

Li, Z., Yu, G., Xu, M., Hu, X., Yang, H., Hu, S., 2016. Progress in studies on river morphodynamics in Qinghai-Tibet Plateau. Advances In Water Science 27, 617–628. https://doi.org/10.14042/j.cnki.32.1309.2016.04.017

Limaye, A.B., 2020. How Do Braided Rivers Grow Channel Belts? Journal of Geophysical Research: Earth Surface 125, e2020JF005570. https://doi.org/10.1029/2020JF005570

Liu, G., Fan, J., Zhao, F., Mao, K., 2017. Monitoring elevation change of glaciers on Geladandong Mountain using TanDEM-X SAR interferometry. J. Mt. Sci. 14, 859–869. https://doi.org/10.1007/s11629-016-3992-5

Liu, X., Zhang, J., Zhu, X., Pan, Y., Liu, Y., Zhang, D., Lin, Z., 2014. Spatiotemporal changes in vegetation coverage and its driving factors in the Three-River Headwaters Region during 2000-2011. J. Geogr. Sci. 24, 288–302. https://doi.org/10.1007/s11442-014-1088-0

Liu, Z., Yao, Z., Wang, R., 2016. Contribution of glacial melt to river runoff as determined by stable isotopes at the source region of the Yangtze River, China. Hydrol. Res. 47, 442–453. https://doi.org/10.2166/nh.2015.089

Lu, H., Li, Z., Hu, X., Chen, B., You, Y., 2022. Morphodynamic processes in a large gravel-bed braided channel in response to runoff change: a case study in the Source Region of Yangtze River. Arab J Geosci 15, 377. https://doi.org/10.1007/s12517-022-09641-y

Luo, Y., Qin, N., Pang, Y., Wang, C., Liu, J., Li, J., Liu, X., 2020. Effect of climate warming on the runoff of source regions of the Yangtze River: take Tuotuo River basin as an example. Journal of Glaciology and Geocryology 42, 952–964.

Lynch, S., 2018. Image Processing with Python, in: Dynamical Systems with Applications Using Python. Springer International Publishing, Cham, pp. 471–489. https://doi.org/10.1007/978-3-319-78145-7_18

Ma, Y., Jiang, C., Long, Y., Li, Z., 2021. Geometrical characteristics of braid channels in the source region of the Yangtze River based on UAV aerial survey data. Journal of Sediment Research 46, 35–41. https://doi.org/10.16239/j.cnki.0468-155x.2021.04.006 (in chinese)

Mann, H.B., 1945. Nonparametric Tests Against Trend. Econometrica 13, 245. https://doi.org/10.2307/1907187

Monegaglia, F., Zolezzi, G., Güneralp, I., Henshaw, A.J., Tubino, M., 2018. Automated extraction of meandering river morphodynamics from multitemporal remotely sensed data. Environmental Modelling & Software 105, 171–186. https://doi.org/10.1016/j.envsoft.2018.03.028

Nicolaou, A., Ingold, R., Liwicki, M., 2014. Binarization with the Local Otsu Filter, in: Lamiroy, B., Ogier, J.-M. (Eds.), Graphics Recognition. Current Trends and Challenges, Lecture Notes in Computer Science. Springer, Berlin, Heidelberg, pp. 176–190. https://doi.org/10.1007/978-3-662-44854-0_14

Otsu, N., 1979. A Threshold Selection Method from Gray-Level Histograms. IEEE Transactions on Systems, Man, and Cybernetics 9, 62–66. https://doi.org/10.1109/TSMC.1979.4310076

Panda, A., Sahu, N., 2019. Trend analysis of seasonal rainfall and temperature pattern in Kalahandi, Bolangir and Koraput districts of Odisha, India. Atmospheric Science Letters 20, e932. https://doi.org/10.1002/asl.932

1309 Peirce, S., Ashmore, P., Leduc, P., 2018. The variability in the morphological active width: Results from
1310 physical models of gravel-bed braided rivers: Morphological active width: physical models of braided
1311 rivers. Earth Surf. Process. Landforms 43, 2371–2383. https://doi.org/10.1002/esp.4400
1312 Pekel, J.-F., Cottam, A., Gorelick, N., Belward, A.S., 2016. High-resolution mapping of global surface water
1313 and its long-term changes. Nature 540, 418–422. https://doi.org/10.1038/nature20584
1314 Qi, D., Li, Y., Chen, Y., Zhao, X., Zhou, C., 2015. Changing characteristics and cause analysis of the runoff in
1315 the source regions of the Yangtze River under the background of climate change. Journal of Glaciology
1316 and Geocryology 37, 1075–1086.
1317 Rowland, J., Shelef, E., Pope, P., Muss, J., Gangodagamage, C., Brumby, S., Wilson, C., 2016. A morphology
1318 independent methodology for quantifying planview river change and characteristics from remotely sensed
1319 imagery. Remote Sensing of Environment 184, 212–228. https://doi.org/10.1016/j.rse.2016.07.005
1320 Sakai, A., Fujita, K., 2017. Contrasting glacier responses to recent climate change in high-mountain Asia. Sci
1321 Rep 7, 13717. https://doi.org/10.1038/s41598-017-14256-5
1322 Schuurman, F., Ta, W., Post, S., Sokolewicz, M., Busnelli, M., Kleinhans, M., 2018. Response of braiding
1323 channel morphodynamics to peak discharge changes in the Upper Yellow River: RESPONSE TO PEAK
1324 DISCHARGE IN BRAIDING YELLOW RIVER. Earth Surf. Process. Landforms 43, 1648–1662.
1325 https://doi.org/10.1002/esp.4344
1326 Sen, P.K., 1968. Estimates of the Regression Coefficient Based on Kendall's Tau. Journal of the American
1327 Statistical Association 63, 1379–1389. https://doi.org/10.1080/01621459.1968.10480934
1328 Shampa, Ali, M.M., 2019. Interaction between the braided bar and adjacent channel during flood: a case study
1329 of a sand-bed braided river, Brahmaputra–Jamuna. Sustain. Water Resour. Manag. 5, 947–960.
1330 https://doi.org/10.1007/s40899-018-0269-x
1331 Singh, K.V., Setia, R., Sahoo, S., Prasad, A., Pateriya, B., 2015. Evaluation of NDWI and MNDWI for
1332 assessment of waterlogging by integrating digital elevation model and groundwater level. Geocarto
1333 International 30, 650–661. https://doi.org/10.1080/10106049.2014.965757
1334 Smith, L.C., Isacks, B.L., Bloom, A.L., Murray, A.B., 1996. Estimation of Discharge From Three Braided
1335 Rivers Using Synthetic Aperture Radar Satellite Imagery: Potential Application to Ungaged Basins. Water
1336 Resources Research 32, 2021–2034. https://doi.org/10.1029/96WR00752
1337 Sonke, W., Kleinhans, M.G., Speckmann, B., van Dijk, W.M., Hiatt, M., 2022. Alluvial connectivity in multi-
1338 channel networks in rivers and estuaries. Earth Surface Processes and Landforms 47, 477–490.
1339 https://doi.org/10.1002/esp.5261
1340 Sun, C., Xu, X., Zhao, T., Yao, T., Zhang, D., Wang, N., Ma, Y., Ma, W., Chen, B., Zhang, S., Cai, W., 2022.
1341 Distinct impacts of vapor transport from the tropical oceans on the regional glacier retreat over the
1342 Qinghai-Tibet Plateau. Science of The Total Environment 823, 153545.
1343 https://doi.org/10.1016/j.scitotenv.2022.153545
1344 Surian, N., Fontana, A., 2017. The Tagliamento River: The Fluvial Landscape and Long-Term Evolution of a
1345 Large Alpine Braided River, in: Soldati, M., Marchetti, M. (Eds.), Landscapes and Landforms of Italy,
1346 World Geomorphological Landscapes. Springer International Publishing, Cham, pp. 157–167.
1347 https://doi.org/10.1007/978-3-319-26194-2_13
1348 Talukdar, S., Pal, S., 2019. Effects of damming on the hydrological regime of Punarbhaba river basin wetlands.
1349 Ecological Engineering 135, 61–74. https://doi.org/10.1016/j.ecoleng.2019.05.014
1350 Wang, C., Yang, T., Xu, A., Ji, Q., G.Ghebrezgabher, M., 2017a. Remote Sensing Monitoring of Glacier
1351 Changes in the Western Region of Tanggula Mountains in Recent 25 Years. Advance in Earth Sciences 32,

101–109.

Wang, G., Hu, H., Li, T., 2009. The influence of freeze–thaw cycles of active soil layer on surface runoff in a permafrost watershed. Journal of Hydrology 375, 438–449. https://doi.org/10.1016/j.jhydrol.2009.06.046

Wang, Q., Ju, Q., Wang, Y., Fu, X., Zhao, W., Du, Y., Jiang, P., Hao, Z., 2022. Regional Patterns of Vegetation Dynamics and Their Sensitivity to Climate Variability in the Yangtze River Basin. Remote Sens. 14, 5623. https://doi.org/10.3390/rs14215623

Wang, R., Yao, Z., Liu, Z., Wu, S., Jiang, L., Wang, L., 2015. Snow cover variability and snowmelt in a high-altitude ungauged catchment: SNOW COVER CHANGE AND SNOWMELT CONTRIBUTION TO RUNOFF. Hydrol. Process. 29, 3665–3676. https://doi.org/10.1002/hyp.10472

Wang, R., Yao, Z., Wu, S., Liu, Z., 2017b. Glacier retreat and its impact on summertime run-off in a high-altitude ungauged catchment. Hydrol. Process. 31, 3672–3681. https://doi.org/10.1002/hyp.11287

Worden, J., de Beurs, K., 2020. Surface water detection in the Caucasus. International Journal of Applied Earth Observation and Geoinformation 91, 102159. https://doi.org/10.1016/j.jag.2020.102159

Wu, S., Yao, Z., Huang, H., Liu, Z., Chen, Y., 2013. Glacier retreat and its effect on stream flow in the source region of the Yangtze River. J. Geogr. Sci. 23, 849–859. https://doi.org/10.1007/s11442-013-1048-0

Xu, H., 2006. Modification of normalised difference water index (NDWI) to enhance open water features in remotely sensed imagery. International Journal of Remote Sensing 27, 3025–3033. https://doi.org/10.1080/01431160600589179

Yan, X., Zhou, Y., Yao, S., Liu, X., 2020. Study on the influence of different land cover types on runoff and sediment transport in the source region of the Yangtze River. Journal of Sediment Research 45, 45–51. https://doi.org/10.16239/j.cnki.0468-155x.2020.04.008

Yang, J., Ding, Y., Liu, S., Lu, A., Chen, R., 2003. Glacier change and its effect on surface runoff in the source regions of the Yangtze and Yellow rivers. Journal of Natural Resources 595-602+645.

Yang, Z., Gao, J., Zhou, C., Shi, P., Zhao, L., Shen, W., Ouyang, H., 2011. Spatio-temporal changes of NDVI and its relation with climatic variables in the source regions of the Yangtze and Yellow rivers. J. Geogr. Sci. 21, 979–993. https://doi.org/10.1007/s11442-011-0894-x

Yao, T., 2019. Tackling on environmental changes in Tibetan Plateau with focus on water, ecosystem and adaptation. Science Bulletin 64, 417. https://doi.org/10.1016/j.scib.2019.03.033

Yao, T., Bolch, T., Chen, D., Gao, J., Immerzeel, W.W., Piao, S., Su, F., Thompson, L., Wada, Y., Wang, L., Wu, G., Xu, B., Yang, W., Zhang, G., Zhao, P., 2022. The imbalance of the Asian water tower. Nature Reviews Earth & Environment 3, 1–15. https://doi.org/10.1038/s43017-022-00299-4

You, Y., Li, Z., Gao, P., Hu, T., 2022. Impacts of dams and land-use changes on hydromorphology of braided channels in the Lhasa River of the Qinghai-Tibet Plateau, China. International Journal of Sediment Research 37, 214–228. https://doi.org/10.1016/j.ijsrc.2021.07.003

Yu, G., Brierley, G., Huang, H.Q., Wang, Z., Blue, B., Ma, Y., 2014. An environmental gradient of vegetative controls upon channel planform in the source region of the Yangtze and Yellow Rivers. CATENA 119, 143–153. https://doi.org/10.1016/j.catena.2014.02.010

Zhang, Y., Liu, S., Xu, J., Shangguan, D., 2008. Glacier change and glacier runoff variation in the Tuotuo River basin, the source region of Yangtze River in western China. Environ Geol 56, 59–68. https://doi.org/10.1007/s00254-007-1139-2

Zhao, Z., Liu, L., Wang, Z., Zhang, Y., Li, L., Liu, F., 2020. Dynamic Changes of Plateau Wetlands in the Damqu River Basin, Yangtze River Source Region, China, 1988-2015. Wetlands 40, 1409–1424. https://doi.org/10.1007/s13157-020-01271-y

Zhu, H., Li, C., Zhang, L., Shen, J., 2015. River Channel Extraction From SAR Images by Combining Gray and Morphological Features. Circuits Syst Signal Process 34, 2271–2286. https://doi.org/10.1007/s00034-014-9922-2

Figure Captions

Figure 1. Location of braided reaches in the SRYR. (a) Study reach of each braided river and its catchment area, the sub-basins. The study reaches were named according to the name of the river, in which the upper, middle and lower reaches of the Tongtian River were named *TTR_S*, *TTR_M* and *TTR_E* respectively. In addition to the main stream of the Tongtian River, the rest of the study reaches are distributed in four sub-basins, namely, Dangqu, Tuotuo, Beilu, and Chumaer River Basins. (b) The *Test* Reach of *TTR_E* Reach was used to evaluate the accuracy of the new Local Otsu + Lowpath method for extracting braided river water bodies.

Figure 2. Identification of braided river branches by global threshold segmentation method.

Figure 3. Water extraction for braided river with Local Otsu + Lowpath method. (a) *MNDWI* image of braided river, (b) water body calculated by Local Otsu method, and (c) water body calculated by Lowpath method, (d) water extraction results of Local Otsu + Lowpath method.

Figure 4. Comparison of water extraction results between the Local Otsu + Lowpath method and Global Otsu method. (a) Comparison of water extraction results of the Local Otsu + Lowpath method (b) Global Otsu method. (c) Comparison of braiding intensity B_{T3} extracted by the Local Otsu + Lowpath method and Global Otsu method with B_{T3}(Real) value interpreted by the visual interpretation; (d) Comparison of water area ratio R_W between the two methods.

Figure 5. The meteorological change in the SRYR. Spatial distribution of (a) precipitation and (b) air temperature and (c) their variation trends of mean annual temperature and annual precipitation from 1957 to 2020 (mark **, *** denotes the significance level of p<0.05 and p<0.01).

Figure 6. The hydrological variation in the SRYR from 1957 to 2020. (a) annual runoff and (b) annual sediment yield (mark *, *** denotes the significance level of p<0.10 and p<0.01).

Figure 7. The variation rule of braiding intensity. (a) Variation of B_{T3} with R_W in the SRYR (b) Correlation between maximum braiding intensity B_{T3peak} and channel width W.

Figure 8. Correlation between average sandbar area ratio $\overline{R_b}$ and water area ratio R_W of each braided reach in the SRYR (mark *** denotes the significance level of p<0.001).

Figure 9. The correlation between index α, inundation chance $\widetilde{R_W}$ and *NDVI* level of river channel (mark * denotes the significance level of p<0.05).

Figure 1.

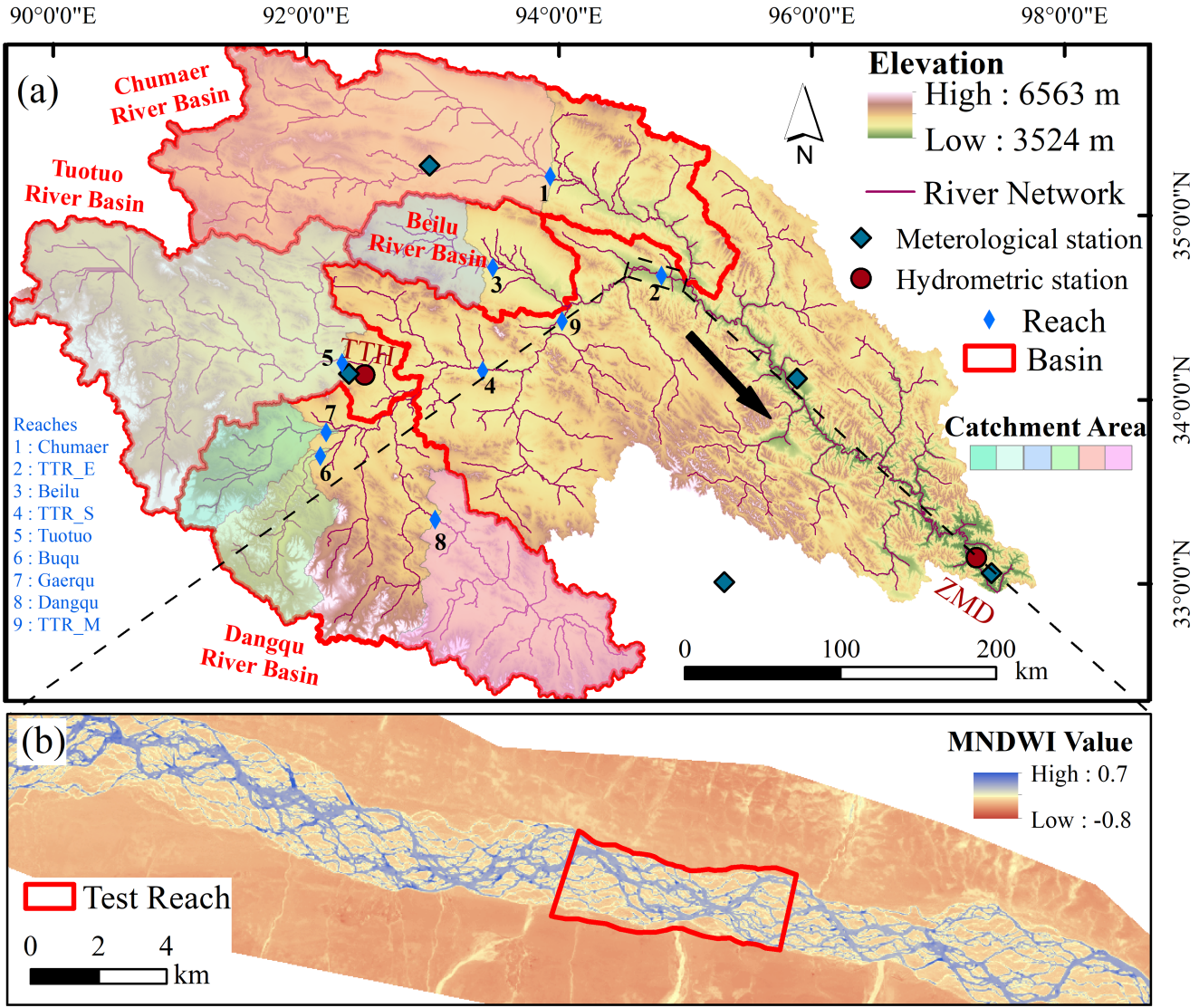
90°0'0"E
92°0'0"E
94°0'0"E
96°0'0"E
98°0'0"E
35°0'0"N
34°0'0"N
33°0'0"N
(a)
Chumaer River Basin
Tuotuo River Basin
Beilu River Basin
Dangqu River Basin
TTH
ZMD
N
Elevation
High : 6563 m
Low : 3524 m
River Network
Meterological station
Hydrometric station
Reach
Basin
Catchment Area
Reaches
1 : Chumaer
2 : TTR_E
3 : Beilu
4 : TTR_S
5 : Tuotuo
6 : Buqu
7 : Gaerqu
8 : Dangqu
9 : TTR_M
0
100
200
km
(b)
MNDWI Value
High : 0.7
Low : -0.8
Test Reach
0
2
4
km

Figure 2.

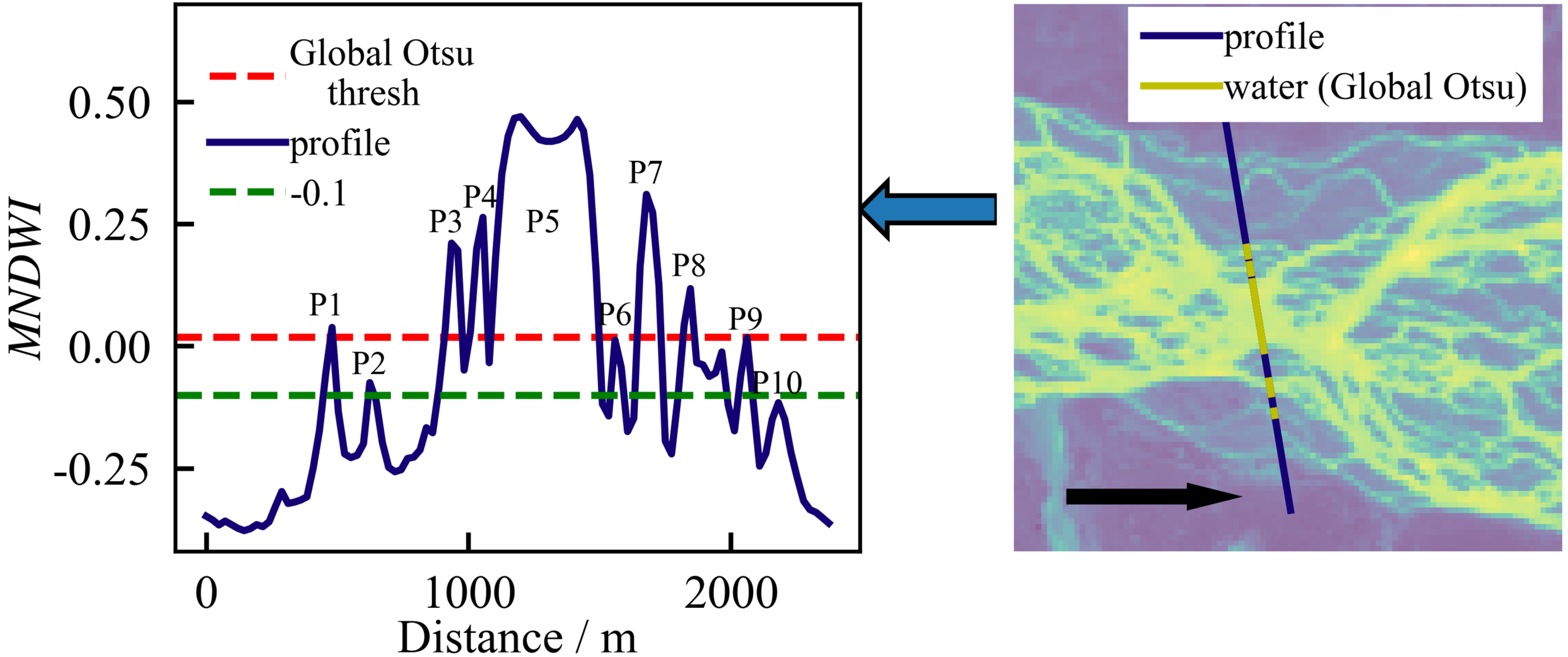
Global Otsu thresh
profile
-0.1
0.50
0.25
0.00
-0.25
MNDWI
P1
P2
P3
P4
P5
P6
P7
P8
P9
P10
0
1000
2000
Distance / m
profile
water (Global Otsu)

Figure 3.

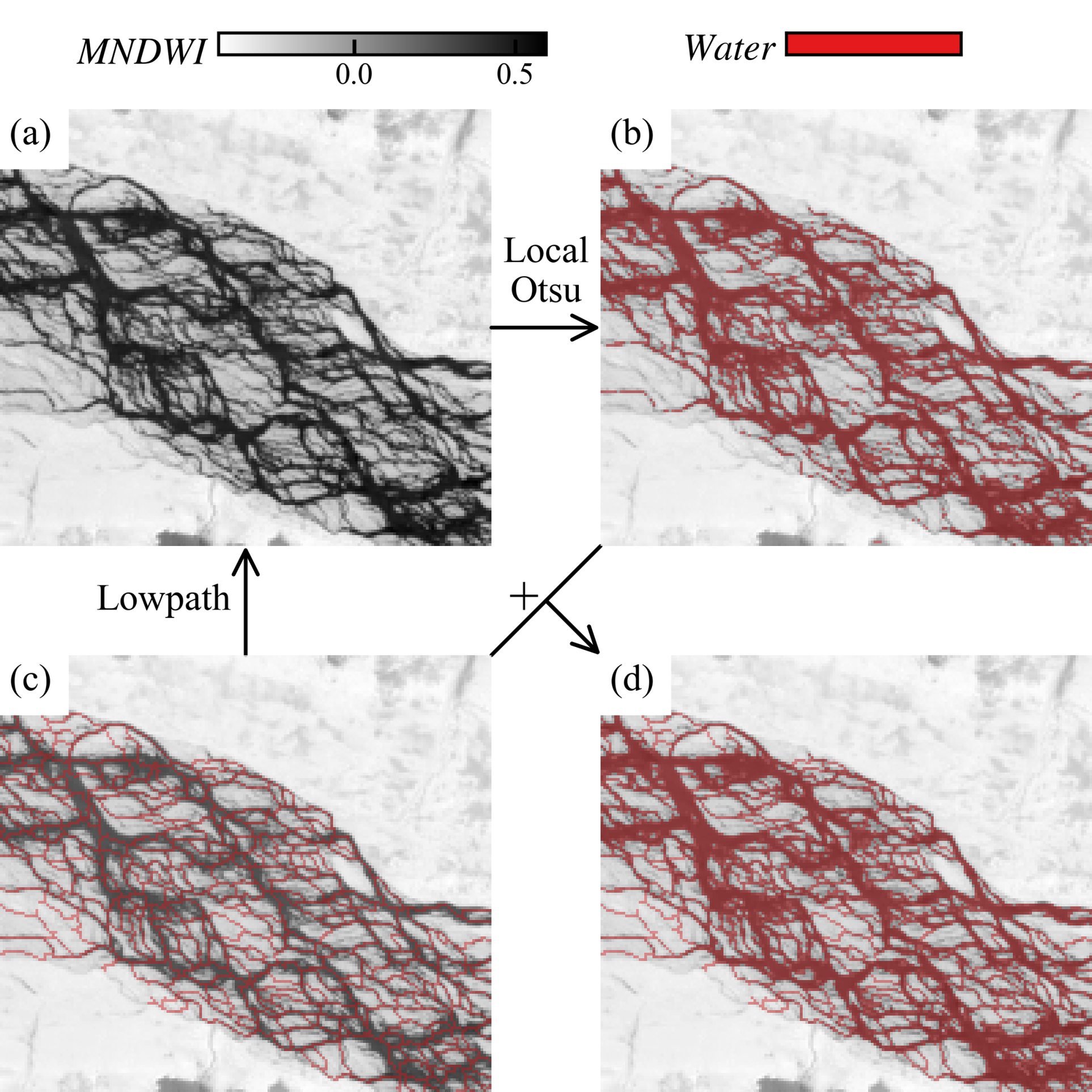
MNDWI
0.0
0.5
Water
(a)
(b)
Local
Otsu
Lowpath
(c)
(d)

Figure 4.

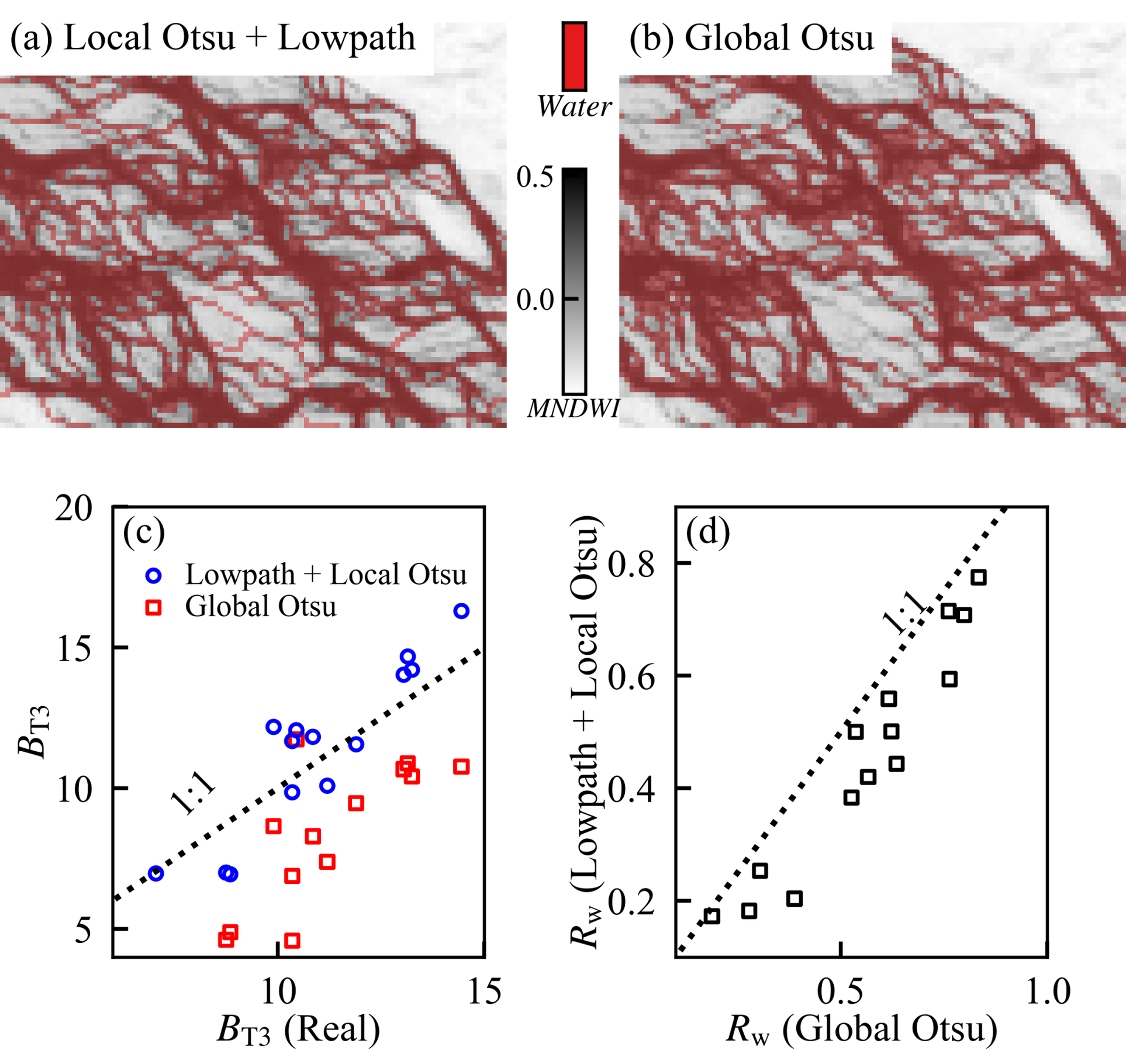
(a) Local Otsu + Lowpath
(b) Global Otsu
Water
0.5
0.0
MNDWI
(c)
Lowpath + Local Otsu
Global Otsu
1:1
B_{T3}
B_{T3} (Real)
20
15
10
5
10
15
(d)
1:1
R_w (Lowpath + Local Otsu)
R_w (Global Otsu)
0.8
0.6
0.4
0.2
0.5
1.0

Figure 5.

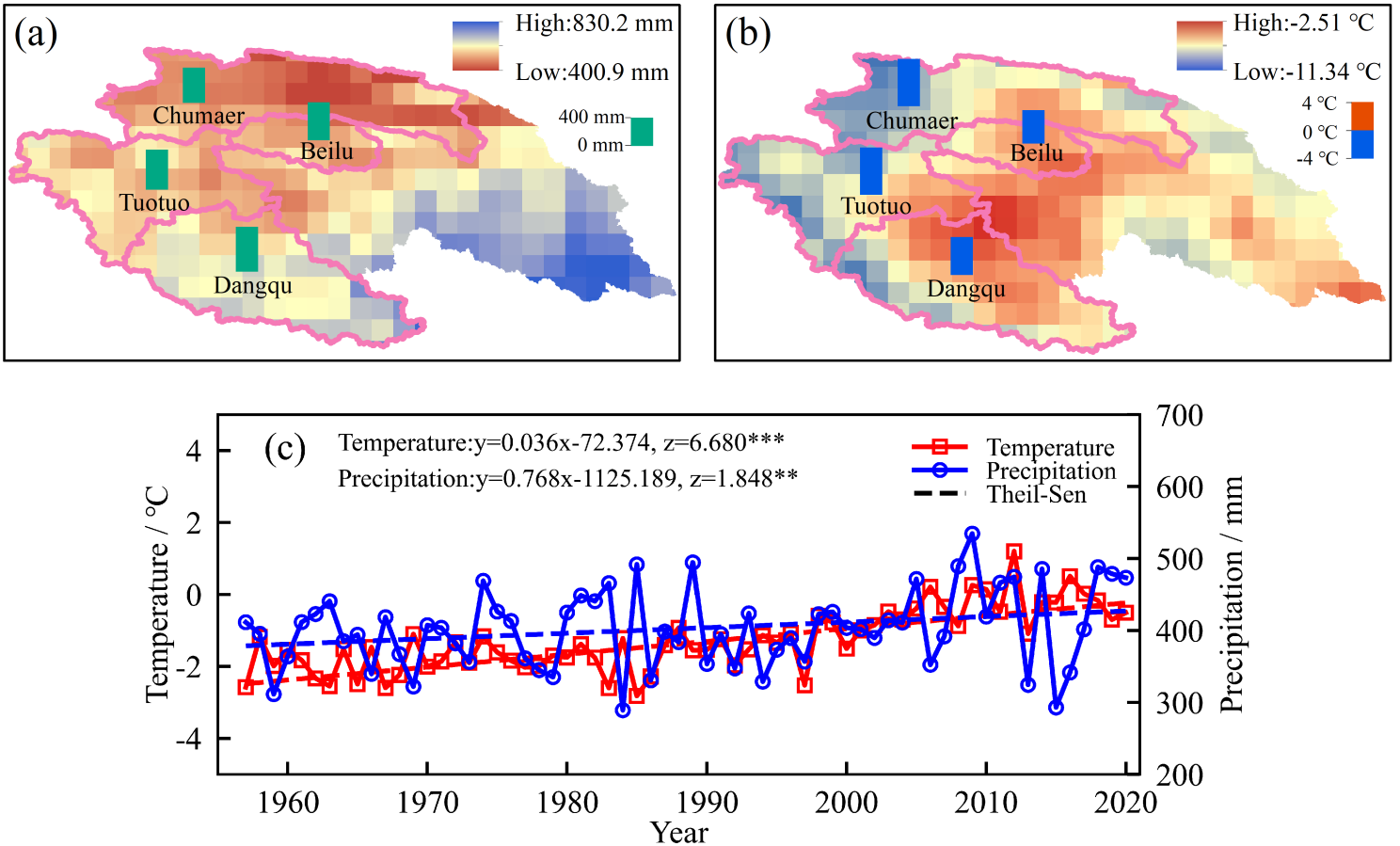
(a)
High:830.2 mm
Low:400.9 mm
400 mm
0 mm
Chumaer
Beilu
Tuotuo
Dangqu
(b)
High:-2.51 ℃
Low:-11.34 ℃
4 ℃
0 ℃
-4 ℃
Chumaer
Beilu
Tuotuo
Dangqu
(c)
Temperature:y=0.036x-72.374, z=6.680***
Precipitation:y=0.768x-1125.189, z=1.848**
Temperature
Precipitation
Theil-Sen
Temperature / ℃
Precipitation / mm
Year
4
2
0
-2
-4
700
600
500
400
300
200
1960
1970
1980
1990
2000
2010
2020

Figure 6.

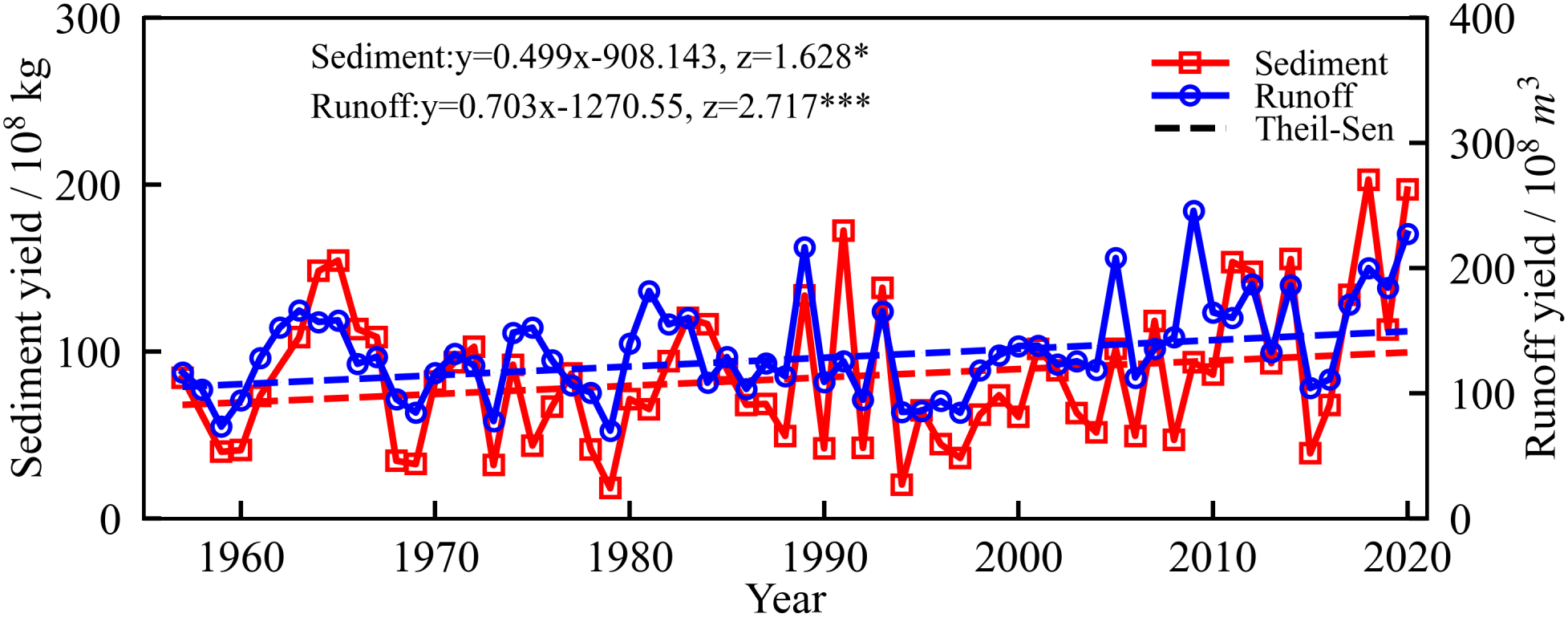
Sediment:y=0.499x-908.143, z=1.628*
Runoff:y=0.703x-1270.55, z=2.717***
Sediment
Runoff
Theil-Sen
Sediment yield / 10^8 kg
Runoff yield / 10^8 m^3
Year
0
100
200
300
400
1960
1970
1980
1990
2000
2010
2020

Figure 7.

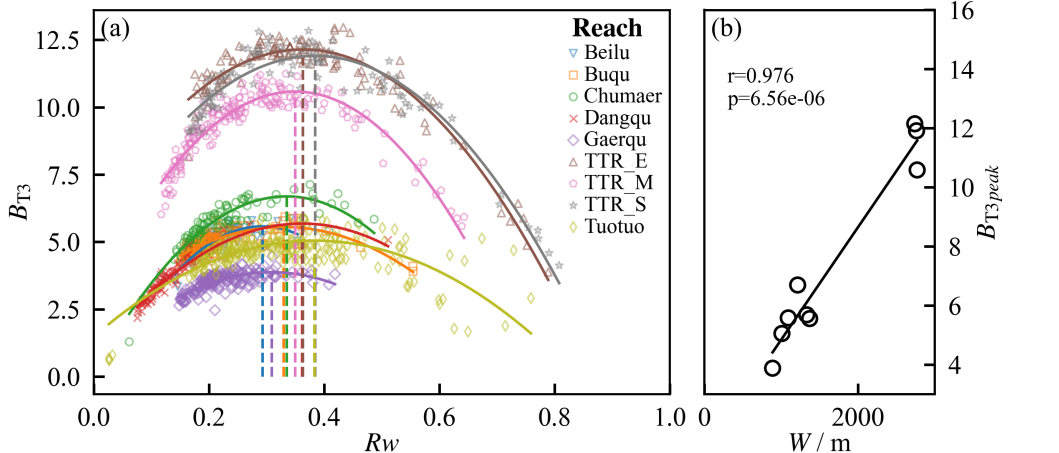
(a)
Reach
Beilu
Buqu
Chumaer
Dangqu
Gaerqu
TTR_E
TTR_M
TTR_S
Tuotuo
B_{T3}
12.5
10.0
7.5
5.0
2.5
0.0
0.0
0.2
0.4
0.6
0.8
1.0
Rw
(b)
r=0.976
p=6.56e-06
16
14
12
10
8
6
4
B_{T3peak}
0
2000
W / m

Figure 8.

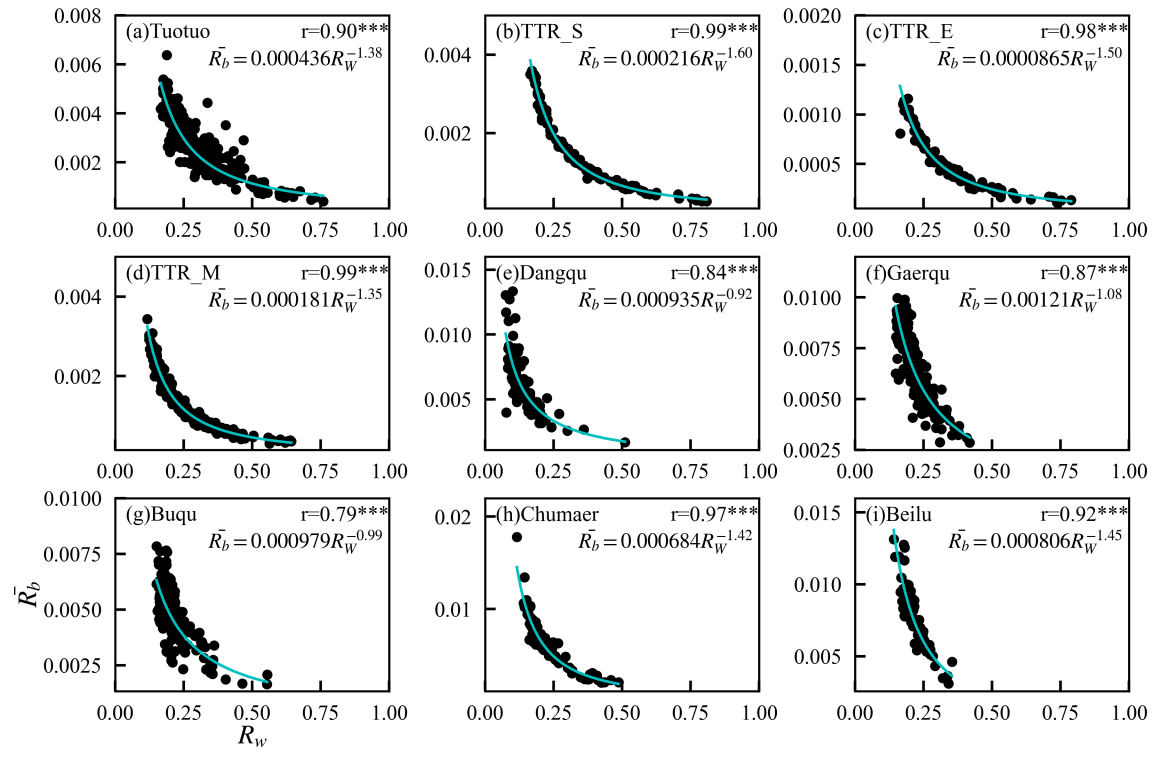
(a)Tuotuo
r=0.90***
$\bar{R_b} = 0.000436 R_W^{-1.38}$
(b)TTR_S
r=0.99***
$\bar{R_b} = 0.000216 R_W^{-1.60}$
(c)TTR_E
r=0.98***
$\bar{R_b} = 0.0000865 R_W^{-1.50}$
(d)TTR_M
r=0.99***
$\bar{R_b} = 0.000181 R_W^{-1.35}$
(e)Dangqu
r=0.84***
$\bar{R_b} = 0.000935 R_W^{-0.92}$
(f)Gaerqu
r=0.87***
$\bar{R_b} = 0.00121 R_W^{-1.08}$
(g)Buqu
r=0.79***
$\bar{R_b} = 0.000979 R_W^{-0.99}$
(h)Chumaer
r=0.97***
$\bar{R_b} = 0.000684 R_W^{-1.42}$
(i)Beilu
r=0.92***
$\bar{R_b} = 0.000806 R_W^{-1.45}$
$\bar{R_b}$
R_w

Figure 9.

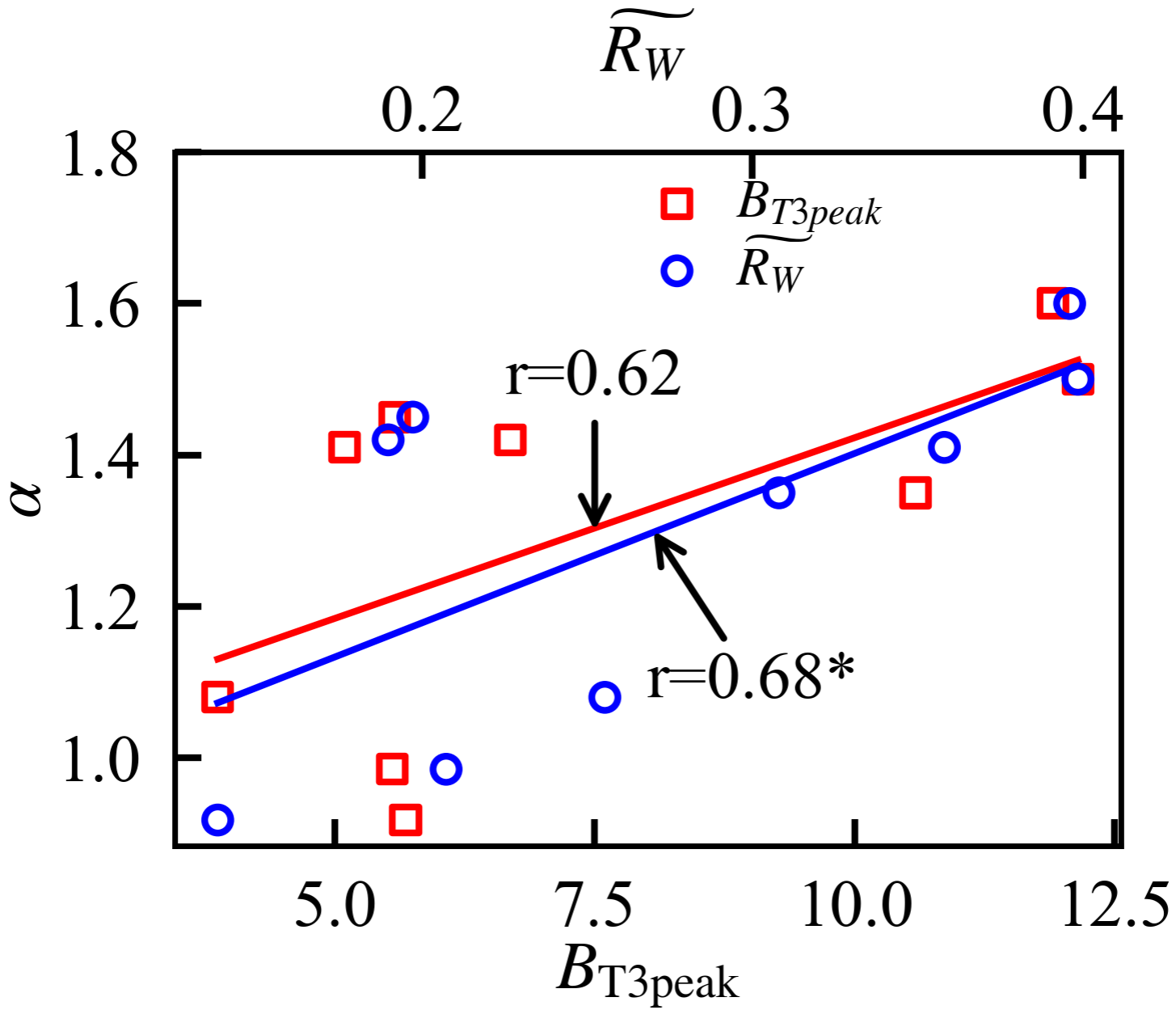
$\widetilde{R_W}$
0.2
0.3
0.4
1.8
1.6
1.4
1.2
1.0
α
B_{T3peak}
$\widetilde{R_W}$
r=0.62
r=0.68*
5.0
7.5
10.0
12.5
B_{T3peak}

Figure 10.

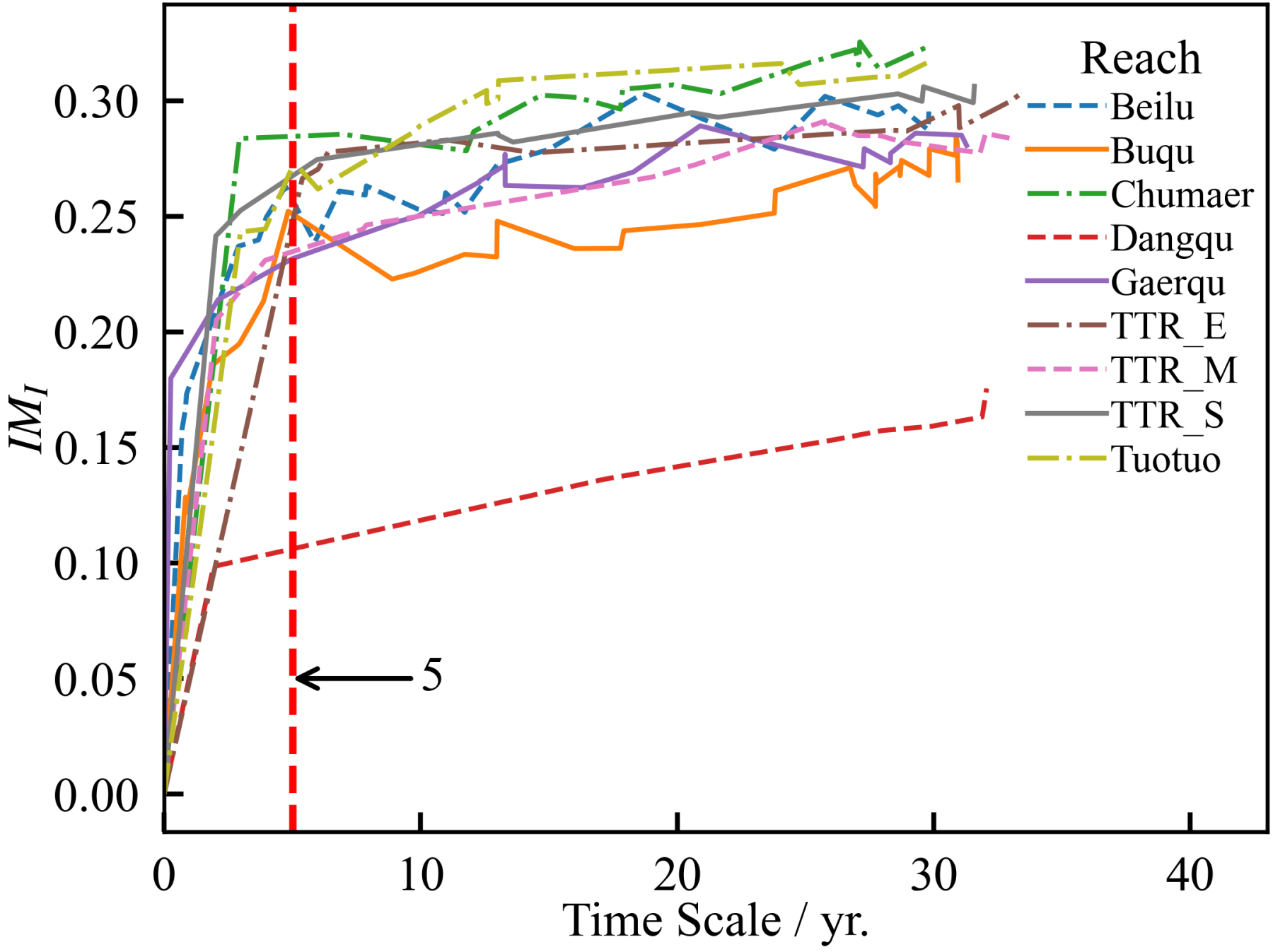
Reach
Beilu
Buqu
Chumaer
Dangqu
Gaerqu
TTR_E
TTR_M
TTR_S
Tuotuo
IM_I
0.30
0.25
0.20
0.15
0.10
0.05
0.00
5
0
10
20
30
40
Time Scale / yr.

Figure 11.

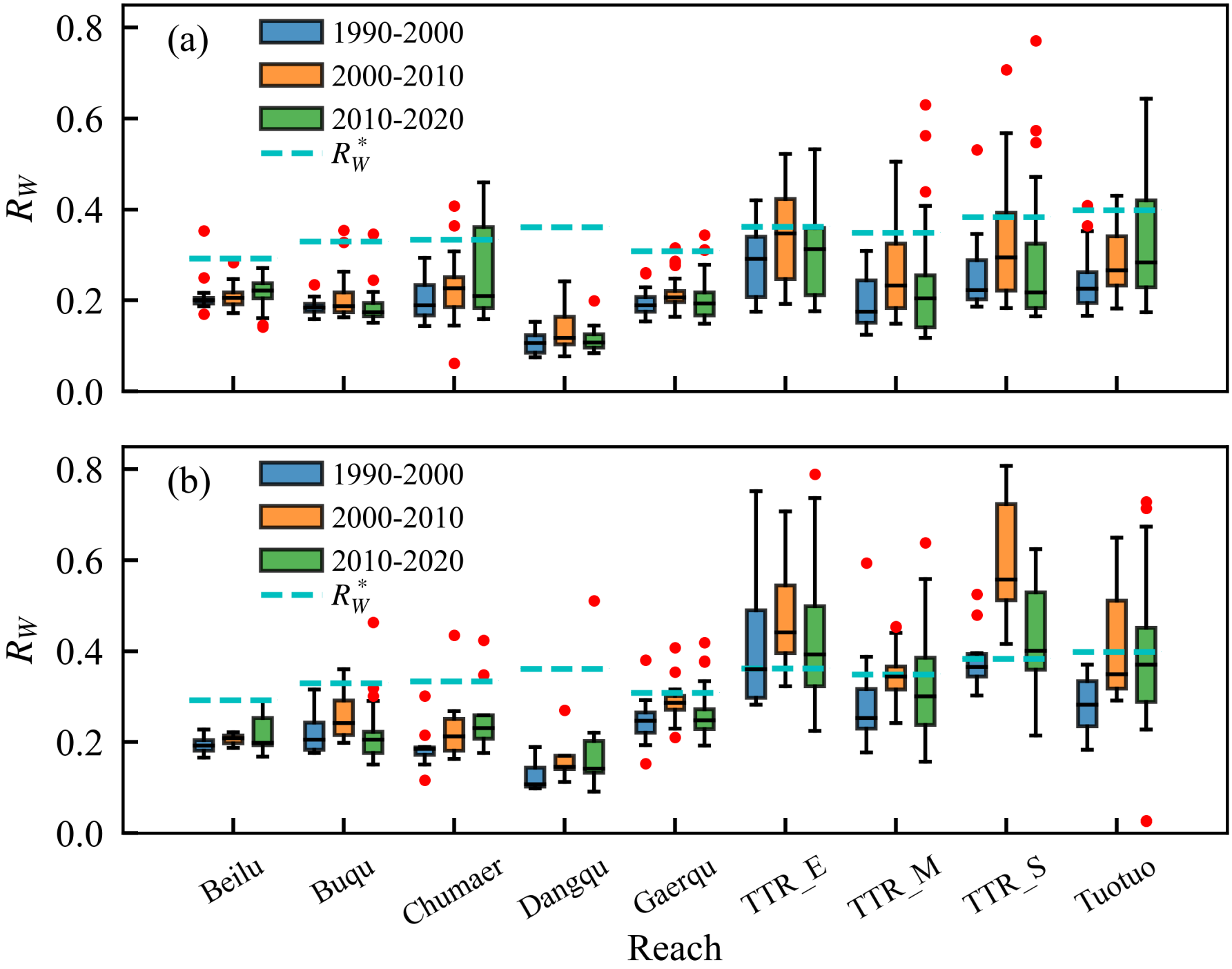
(a)
(b)
1990-2000
2000-2010
2010-2020
R_W^*
R_W
0.0
0.2
0.4
0.6
0.8
Beilu
Buqu
Chumaer
Dangqu
Gaerqu
TTR_E
TTR_M
TTR_S
Tuotuo
Reach

Figure 12.

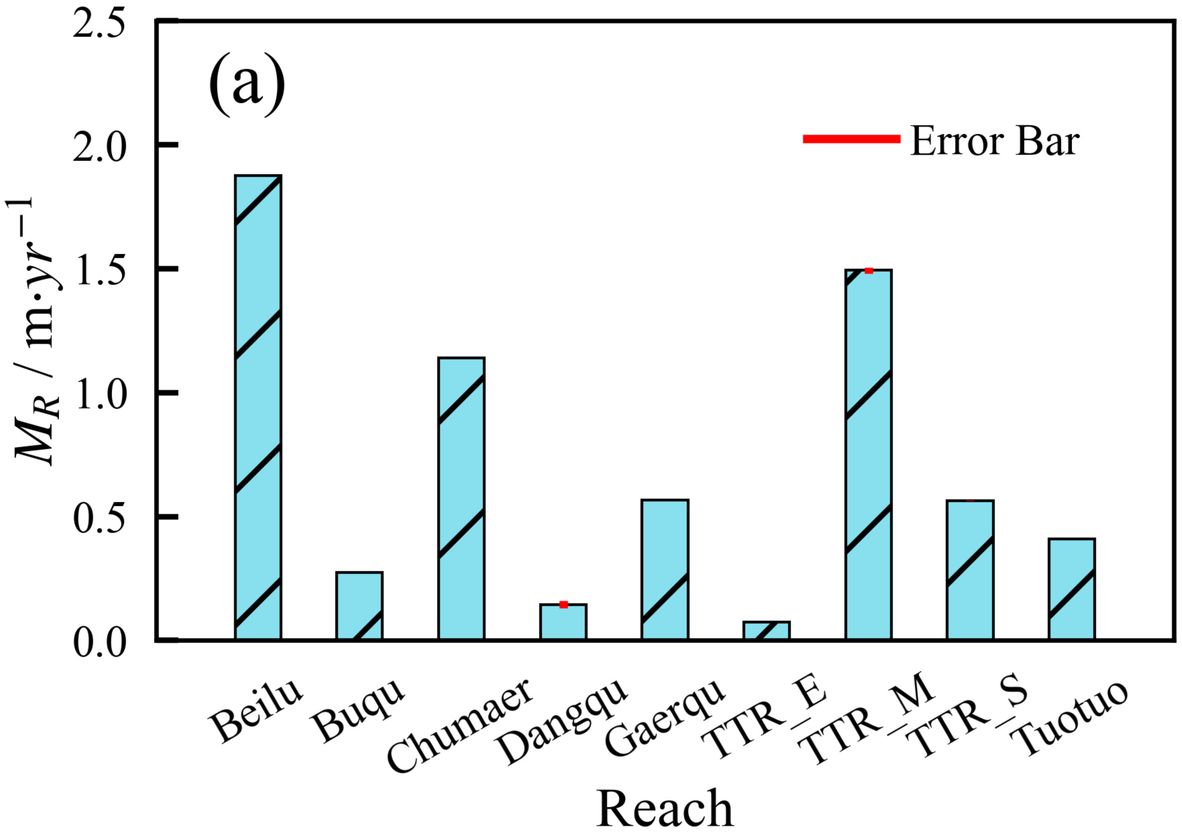
(a)
Error Bar
2.5
2.0
1.5
1.0
0.5
0.0
M_R / m·yr^{-1}
Beilu
Buqu
Chumaer
Dangqu
Gaerqu
TTR_E
TTR_M
TTR_S
Tuotuo
Reach

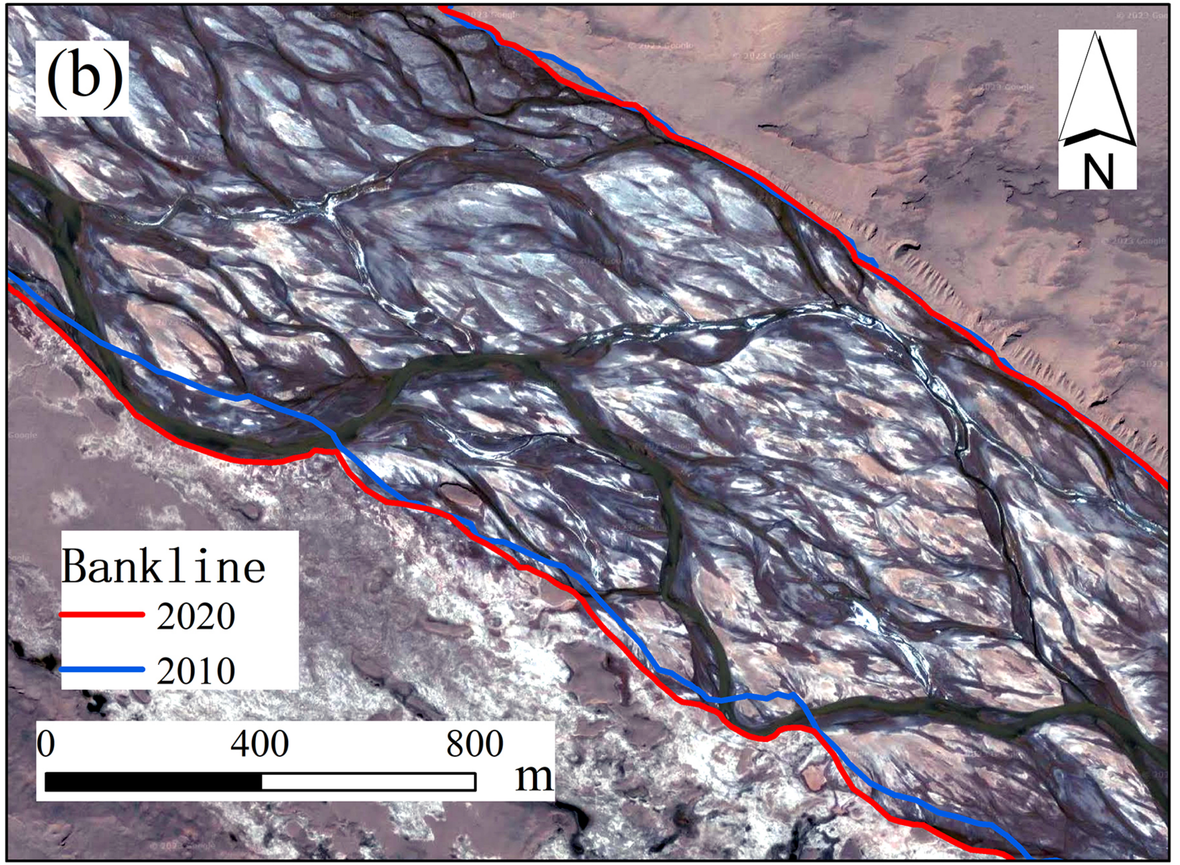
(b)
N
Bankline
2020
2010
0
400
800
m

Figure 13.

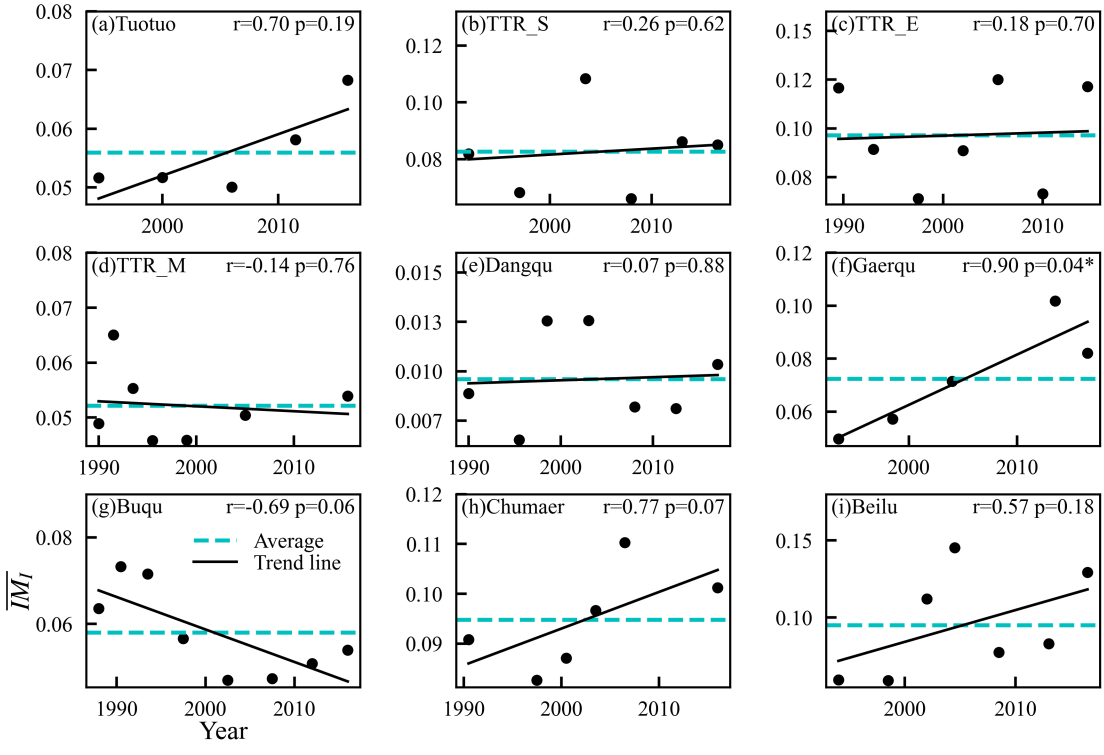
(a)Tuotuo r=0.70 p=0.19
(b)TTR_S r=0.26 p=0.62
(c)TTR_E r=0.18 p=0.70
(d)TTR_M r=-0.14 p=0.76
(e)Dangqu r=0.07 p=0.88
(f)Gaerqu r=0.90 p=0.04*
(g)Buqu r=-0.69 p=0.06
(h)Chumaer r=0.77 p=0.07
(i)Beilu r=0.57 p=0.18
Average
Trend line
$\overline{IM_I}$
Year

Figure 14.

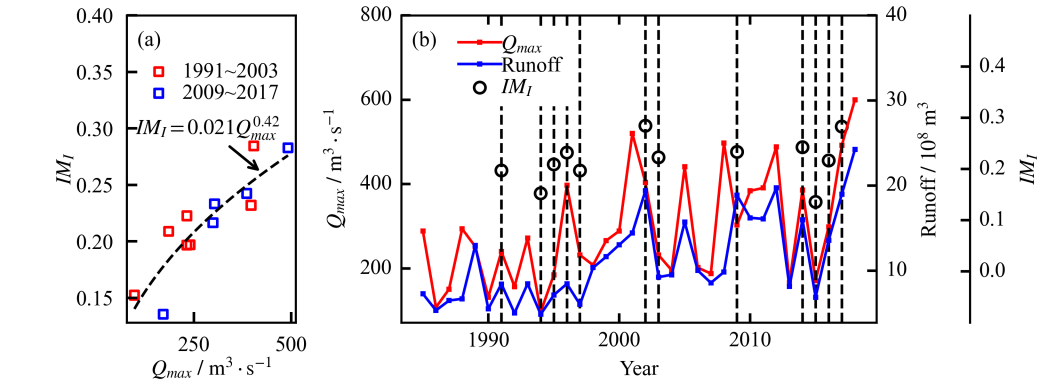
(a)
1991~2003
2009~2017
$IM_I = 0.021 Q_{max}^{0.42}$
IM_I
Q_{max} / m$^3 \cdot$s^{-1}
(b)
Q_{max}
Runoff
IM_I
Q_{max} / m$^3 \cdot$s^{-1}
Runoff / 10^8 m^3
IM_I
Year

Figure 15.

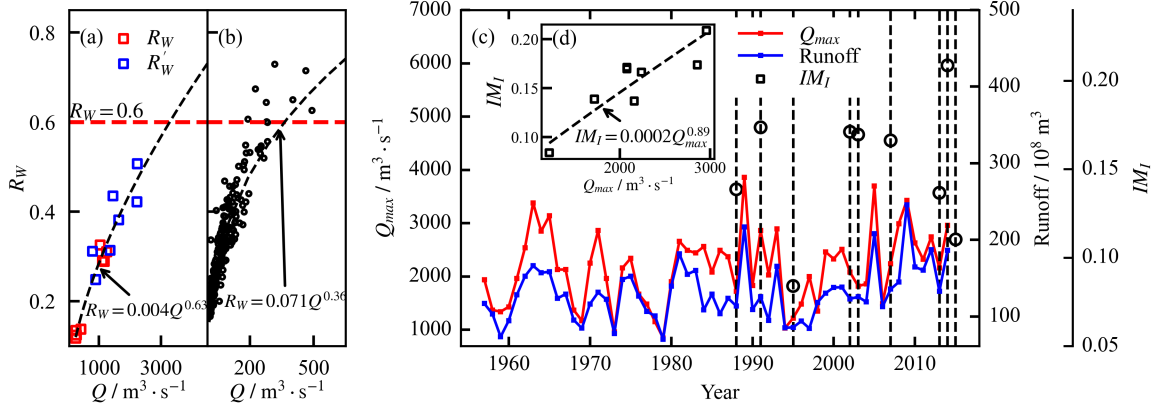
(a)
(b)
(c)
(d)
R_W
R_W'
$R_W = 0.6$
$R_W = 0.004Q^{0.63}$
$R_W = 0.071Q^{0.36}$
Q / m$^3 \cdot$s^{-1}
Q_{max}
Runoff
IM_I
$IM_I = 0.0002Q_{max}^{0.89}$
Q_{max} / m$^3 \cdot$s^{-1}
Runoff / 10^8 m^3
Year

Figure 16.

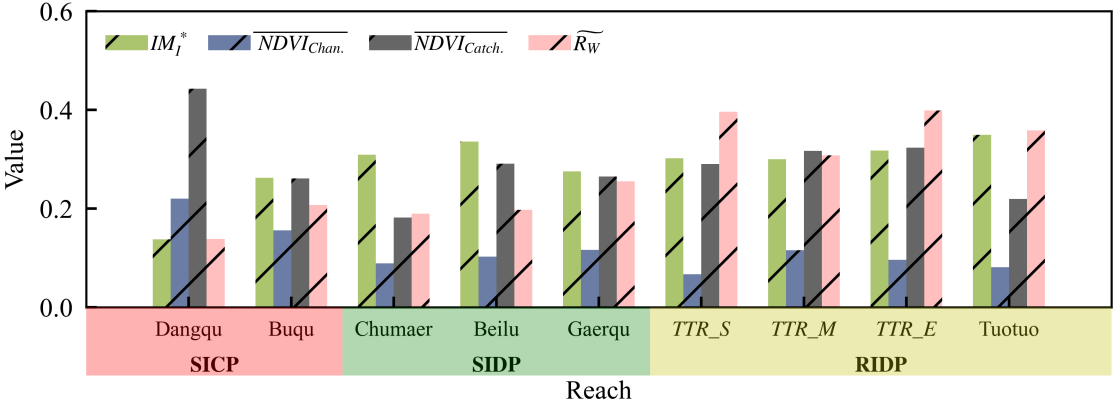
0.6
0.4
0.2
0.0
Value
IM_I^*
$\overline{NDVI_{Chan.}}$
$\overline{NDVI_{Catch.}}$
$\widetilde{R_W}$
Dangqu
Buqu
Chumaer
Beilu
Gaerqu
TTR_S
TTR_M
TTR_E
Tuotuo
SICP
SIDP
RIDP
Reach

Figure 17.

P: *Precipitation*
T: *Temperature*
Q: *Runoff flux*
S: *Sediment flux*
V: *Vegitation abundance in channel & watershed*

↑: *increase*
↓: *decrease*
—: *no trend*

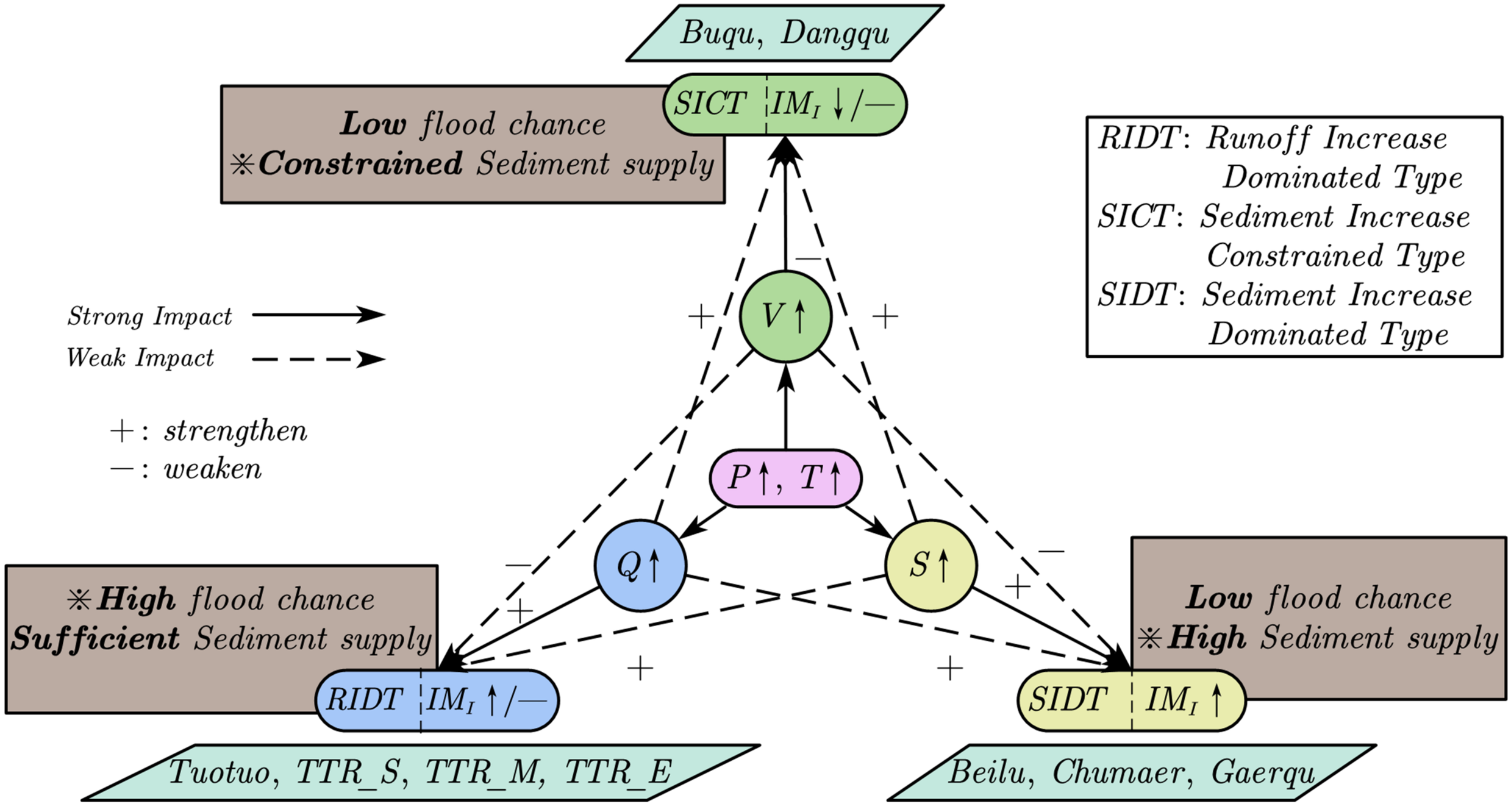

Strong Impact ⟶
Weak Impact - - -⟶

+: *strengthen*
—: *weaken*

RIDT: *Runoff Increase Dominated Type*
SICT: *Sediment Increase Constrained Type*
SIDT: *Sediment Increase Dominated Type*

Table 1 Selection of remote sensing images for each reach.

Reach	$L \times W$ (m)	Landsat + Sentinel			Google Earth (Landsat 7 + Sentinel-2)			
					T_1		T_2	
		Total pics	Resolution /m	Process Time (per pic) /s	Year	Resolution/m	Year	Resolution /m
Beilu	5600×1092	85	30	4.24	2010	0.30	2020	0.30
Buqu	8400×1371	152	30	5.53	2005	0.30	2020	0.30
Chumaer	7400×1215	95	30	5.68	2007	0.30	2020	0.30
Dangqu	9600×1333	95	30	6.32	2000	15 (Landsat 7)	2020	10 (Sentinel-2)
Gaerqu	8000×888	184	30	5.22	2003	0.30	2020	0.30
TTR_E	33000×2740	116	30	19.78	2012	0.30	2020	0.30
TTR_M	16200×2771	178	30	9.87	2000	15 (Landsat 7)	2020	10 (Sentinel-2)
TTR_S	11000×2763	108	30	7.83	2010	0.30	2020	0.30
Tuotuo	18600×1010	245	30	9.04	2003	0.30	2020	0.30

Note: L is the reach length, W is the average reach width.